Earij, A., Alfano, G., Cashell, K.A., Zhou, X. Nonlinear Three–Dimensional Finite–Element Modelling of Reinforced–Concrete Beams: Computational Challenges and Experimental Validation. Engineering Failure Analysis, 2017. http://www.sciencedirect.com/science/article/pii/S1350630717303151

Nonlinear Three–Dimensional Finite–Element Modelling of Reinforced–Concrete Beams: Computational Challenges and Experimental Validation

Alrazi Earij, Giulio Alfano, Katherine Cashell, Xiangming Zhou
Department of Mechanical, Aerospace and Civil Engineering, Brunel University London
Kingston Lane, UB8 3PH, Uxbridge, UK

Abstract

Three–dimensional nonlinear finite–element models have been developed to investigate the loading–unloading–reloading behaviour of two reinforced–concrete beams under four–point bending using explicit dynamics in ABAQUS. The damaged–plasticity model proposed by Lubliner and collaborators was employed for the plain concrete, and elastic–perfectly plastic models were employed for the steel reinforcement. A perfect bond was assumed between the steel rebars and concrete, whereby the bond–slip behaviour, as well as damage along crack patterns, were modelled through concrete damage. The influence of the shape of the tension–softening law on the numerical load–deflection response was studied by considering bi–linear, exponential and linear post–failure stress–displacement and stress–strain relationships. The effect of modelling steel rebars with truss or beam elements was also investigated. Structured meshes of linear hexahedral elements either with incompatible modes or with reduced integration, and unstructured meshes of either linear or 'modified' quadratic tetrahedral elements were considered. In terms of load–deflection curves, both the structured and the unstructured meshes gave results in very good agreement with test results. In terms of crack patterns, results predicted by the structured meshes exhibited some mesh bias, which was less pronounced with the unstructured meshes. In the post–yield phase, if a geometrically nonlinear model is used, discrepancies were found when truss elements were used for steel rebars, whereas good agreement was found if the bending stiffness of the rebars is included using beam elements. This is a non–obvious result that may be important to consider when studying the progressive collapse of RC structures.

Keywords: Nonlinear FEA; reinforced–concrete beams; ABAQUS/explicit; embedded reinforcement; damage–plasticity coupling.

1. Introduction

The structural analysis of reinforced–concrete (RC) beams can be conducted with a great variety of methods, from simplified and well–established methods of RC design suggested in the codes of practice to other more sophisticated methods, which account for damage, plasticity, cracking, bond–slip interaction between steel rebars and concrete. The latter models typically require a numerical solution. For ordinary applications, the complexities entailed by detailed three–dimensional (3D) numerical simulations may make the analysis too expensive in terms of time for setting up the model and obtaining the solution, cost of determining all material parameters and also level of knowledge and expertise required. On the other hand, for special applications, such as in nuclear engineering or in forensic investigations, this increased cost of the simulation can be acceptable (Gentili, Petrini 2016, Solomos, Casadei et al. 2011, Oliveira 2009). Furthermore, for research purposes, detailed and accurate finite–element (FE) models can replace experimental testing and enable the exploration of a much broader range of innovative design solutions, e.g. for strengthening RC beams with fibre–reinforced plastics (FRPs). In all these cases, priority is given to the predicting ability of the models and the accuracy of the solution, but of course the analyses still need to be feasible and the computational cost is an important issue.

To achieve an accurate depiction of the behaviour in modelling RC beams, it is important to consider a large number of complex phenomena including the inelastic and fracture process of concrete and the 'bond–slip' interaction between the steel rebars and surrounding concrete. In turn, an effective bond–slip law should consider a number of complex mechanisms, including but not limited to adhesion, friction, geometry of the ribs of the rebars, if any, localised concrete crushing and damage, and localised cracks.

The complexity of the problem explains the great amount and variety of models proposed in the last three to four decades and their various level of sophistication. The underlying physics of the concrete fracture, induced mainly by tensile cracking, can be better understood using a micromechanics approach, yet at high computational costs especially for large structures and 3D analyses (Gentili, Petrini 2016, Oliveira 2009). On the contrary, the macroscopic approach, in which the principles of continuum mechanics are employed, is widely used to analyse a variety of concrete structures subjected to different types of loading. Elasticity, nonlinear–elasticity, plasticity, fracture mechanics, damage theories have been widely used in this regard. Plasticity–based models allow the modelling of the unrecoverable deformation in concrete loaded in compression. Developing a plasticity–based model requires defining (a) a yield/failure surface to determine the onset of plastic deformation, (b) a flow rule to determine the rate of plastic strains, and (c) a hardening/softening rule to define the evolution of the yield surface with plastic deformation. Many yield criteria, including but not limited to Mohr–Coulomb, Drucker–Prager (1952), Bresler–Pister (1958), William–Warnke (1975), Ottosen (1977) and Hsieh–Ting–Chen (1979), have been proposed to this end. A few studies (Zhu, Tang 2002, Ziraba, Baluch et al. 1995, Buyukozturk 1977) utilised the Mohr–Coulomb model. This is partially because of the irregular hexagon failure surface used in this model, a feature that causes some numerical difficulties. On the contrary, the smooth yield surface of the Drucker–Prager (D–P) model and the simplicity of its implementation make it more desirable in FE studies. Arslan (2007) investigated the sensitivity to the D–P parameters in the case of the shear design of RC beams. Park and Klingner (1997) employed multiple plasticity failure criteria to model the nonlinear behaviour of RC in plane stress. Yu et al. (2010a) conducted a critical review on the capability of existing D–P plasticity models to predict the behaviour of actively– and passively–confined concrete. The review concluded that an accurate prediction for the aforementioned types of concrete could not be achieved using existing D–P models unless three modifications were introduced, which comprised (i) the inclusion of the third deviatoric stress invariant in the yield criterion, (ii) the dependence of the hardening/softening rule and flow rule on the confining pressure and (iii) the dependence of the flow rule on the variation of the confinement.

As for the simulation of cracks in concrete, two approaches are normally used, the discrete–crack approach and the smeared–crack approach. In the former, cracks are modelled as geometrical entities where a displacement discontinuity is allowed. To this end, the size of the fracture process zone (FPZ), the zone of inelastic material behaviour at the crack tip, needs to be considered. Since this size is larger than or comparable with the dimensions of the majority of concrete structures, concrete should be treated as a quasi–brittle material, which requires nonlinear fracture–mechanics methods. For this purpose, cohesive–zone models (CZMs) are typically used, which include the fictitious crack model (FCM) (Hillerborg, Modéer et al. 1976), the first CZM implemented in a FE analysis.

The incorporation of CZMs into a FE analysis can be achieved using, for example, 'zero–thickness' interface elements (Manzoli, Gamino et al. 2012, Yu, Ruiz 2006, Ožbolt, Lettow et al. 2002). Early applications of this approach to the FE analyses of RC were attempted by

Nilson (1968) and Ngo and Scordelis (1967), by introducing interface elements on all inter–element boundaries, although this introduces a spurious compliance that can become an issue for very refined meshes. Furthermore, this approach also forces cracks to follow element boundaries. The introduction of a displacement discontinuity independent of the boundaries of the finite elements, a concept also known as 'strong discontinuity', can be used to alleviate the issue of mesh–dependency encountered when using the discrete crack approach. This idea led to the development of finite–elements with embedded strong discontinuity (E–FEM) (Dvorkin, Cuitiño et al. 1990, Lotfi, Shing 1995, Oliver 1996) and the 'extended finite–element method' (X–FEM) (Belytschko, Moës et al. 2001, Wells, Sluys 2001), which have been used to capture the initiation and propagation of arbitrary cracks in concrete (Unger, Eckardt et al. 2007, Yu, Huang 2008).

The smeared–crack approach (Rashid 1968) treats cracked concrete as a continuous medium, and approximates the discontinuity in the displacement field induced by cracks as localised inelastic strains, whose appearance and evolution are the result of the material nonlinear constitutive relationship. In essence, the material stiffness in the direction of the principal tensile stress (i.e. orthogonal to the crack) at the cracking location is progressively reduced down to or close to zero. Cracks can be represented by using the 'fixed crack' model (Rashid 1968) or the 'rotating crack' model (Jirásek, Zimmermann 1998, Gupta, Akbar 1984, Cope, Rao et al. 1980). In the former representation, once the principal tensile stress exceeds the concrete tensile strength, a crack, whose direction remains unchanged during subsequent loading, forms perpendicular to the direction of the principal tensile stress. Conversely, in the rotating crack model, crack re–orientation with the loading history or material response is allowed, and the crack orientation is assumed normal to the principal tensile strain (Milford, Schnobrich 1985, Foster, Budiono et al. 1996).

One issue associated with the use of the smeared–crack concept is the tendency of inelastic strains to localise along one row of finite–elements (Bažant 1976). If this is not taken properly into account, the energy dissipation depends on the element size and tends to zero when the mesh is indefinitely refined (Bažant 1980). The introduction of a 'localisation limiter' alleviates the mesh non–objectivity issue and prevents the strain softening from being localised in an infinitesimally small region. This can be done with nonlocal or gradient models, in which, the stress at a point depends either on the strains both at the same point and in a suitably defined neighbourhood of it (nonlocal approach) or on the strain and the successive gradients of the strain tensor at that point (gradient approach) (Bažant 1986). The 'crack band model' is another simpler localisation limiter, which alleviates the dependency of the concrete fracture energy on the element size by relating such size to the concrete constitutive relationship. This can be achieved by associating the strain–softening law with a certain characteristic width, h_c, of the crack band (Bažant, Planas 1998). The salient attribute of the crack band localisation limiter, once implemented in a smeared–crack model, is that the post–failure stress versus crack–opening curve (of the discrete–crack model) and stress versus cracking–strain curve (of the smeared–crack model) will coincide if the crack–opening displacement is taken as $w_c = h_c\varepsilon_{cr}$, ε_{cr} being the cracking–strain (Bažant, Planas 1998).

Ultimately, in a two–dimensional (2D) or 3D FE simulation of RC beams, both the smeared– and discrete–crack approaches allow simulating the formation and propagation of multiple cracks developing within an RC beam and, therefore, can capture the so–called 'tension stiffening'. This term is used to indicate the ability of the uncracked concrete between two cracked cross–sections to resist tensile stresses, which are transferred to the concrete by the residual bond between the steel rebars and concrete. This results in an overall bending stiffness of the RC beam, which is higher than that computed by considering the stiffness provided by the cracked cross–section only. However, if the discrete–crack approach is used, two additional ingredients must be implemented, namely a crack initiation criterion and a bond–slip law at the steel–concrete interface. The latter may, for example, be introduced using interface elements between the rebars and concrete. Instead, with a smeared–crack approach, the initiation criterion is embedded in the constitutive law, and the bond–slip is automatically captured, too, by continuum damage in the finite–elements adjacent to the steel rebars. Therefore, no additional bond–slip law and interface elements are needed.

To the authors' knowledge, the work by Suidan and Schnobrich (1973) is the earliest study reporting a 3D FE analysis of RC beams where 20–noded isoparametric brick elements were employed. Since then, many 2D and 3D FE models have been developed to investigate the nonlinear behaviour of RC beams. Plain stress (Jankowiak 2012, Chen, Teng et al. 2011, Chen, Chen et al. 2012, Zangeneh Kamali 2012, Nilforoush Hamedani, Shahrokh Esfahani 2012) and plain strain elements (Sümer, Aktas 2011, Yang, Chen 2005, Coronado, Lopez 2006) were used to model concrete in the 2D scenario. Different types of elements have been used to model the concrete in the 3D case such as 8–noded brick elements (Głodkowska, Ruchwa 2010, Sinaei, Shariati et al. 2012, Cervantes 2013, Jiang, Wang et al. 2012, Wang, Xu 2011), 20–noded brick elements (Radfar, Foret et al. 2012) both with reduced integration, and 4–noded linear tetrahedral elements (Obaidat, Heyden et al. 2010, Obaidat, Dahlblom et al. 2010). For concrete, to the best of the authors' knowledge, the use of 3D 8–noded solid elements with incompatible modes has never been reported in the literature in the case of 3D nonlinear FE analyses of RC beams up to failure. This is despite the fact that these elements, based on the pioneering 'enhanced strain' method by Simo and Rifai (1990) (initially in 2D elements), are known to provide better computational performance in flexure–dominated problems than conventional 8–noded elements.

Apart from the work reported by Radfar, Foret and Sab (2012), in which steel rebars were modelled using 3D 20–noded brick elements with reduced integration, the aforementioned models used 2–noded truss elements to model steel rebars. The literature reported only two recent studies (Markou, Papadrakakis 2012, Ahmed 2014), in which 3D beam elements were employed to model the steel reinforcement. Furthermore, none of the above studies has addressed cases including unloading and reloading.

This paper focuses on detailed nonlinear 3D FE simulations of RC beams using a smeared–crack model, namely the 'concrete damaged–plasticity' (CDP) model implemented in the commercial code ABAQUS (Dassault Systèmes 2014a), and an explicit–dynamics solution procedure. Although the studied beams could be simulated using 2D models, it was deemed useful to use 3D models instead for following reasons. Firstly, the assumptions of plane stress and plane strain used in 2D models are not entirely valid for typical beam sizes, and it is difficult to estimate a priori the extent to which the predictivity of the 2D models can be affected by the use of one of these assumptions. Secondly, the RC beams presented here form part of an extensive experimental and numerical investigation, in which these beams are later retrofitted with FRPs. Since this strengthening technique is not typically applied to the entire beam width, 3D effects can rise and the estimation of these effects and their impacts on the computed results become none–trivial.

Even when 2D nonlinear models can lead to sufficiently good predictions, for all the above reasons they require significant experience and engineering judgement. Therefore, a cost/benefit analysis can reveal, in some cases, that the significantly larger computational cost of a 3D analysis can be compensated by the greater speed of creating the model (also considering that this step can be considerably automated and parametrised) and by the efficiency of managing the transfer of knowledge within large engineering and research organisations. Last but not least, the computational cost of 3D analysis is bound to significantly decrease in the next 5 to 10 years thanks to the advances in computational methods, hardware performance and parallel computing. This will likely further shift the focus from 2D to 3D analyses in the future.

The paper aims at addressing three main areas where, as discussed in the above literature review, open questions remain for an analyst wishing to conduct these types of numerical simulations. One is the influence of the element types on the FE results. In particular, the performance of 3D solid elements with incompatible modes, never considered so far, is assessed and compared with that of 8–noded elements with reduced integration, with fully integrated 20–noded elements and with linear and quadratic tetrahedral elements.

The second question that is aimed to be addressed in this work is whether the bending stiffness of the steel rebars can be neglected, as is done in most of the studies in the literature, or if this assumption has a significant influence on the structural response. To this end, both 3D truss elements and 3D beam elements are considered in the analyses and the differences in results are discussed.

The third open issue (Oliver, Linero et al. 2008) is whether the concrete–damaged plasticity model leads to effective predictions not only in the loading phase but also during unloading.

To investigate these three main aspects, the FE results are validated against the experimental results reported by Alfano et al. (2012), which included tests on two RC control beams subject to 4–point bending. The beams were casted using the same concrete and rebar types and varied in length and cross–sectional area. Therefore, in addition to the above–discussed main novel aspects of the investigation, the rationale used for the determination of material parameters and for the assessment of the predicting capability of the CDP model are further non–straightforward aspects, which are addressed in this paper. Another aspect that has received little attention is the implications of basing the CDP model on a uniaxial stress–relative displacement law or a uniaxial stress–strain law. These are related through the crack–band concept, and therefore, they should provide the same results in the exact solution of the boundary–value problem. However, in practice the localisation limiter, i.e. the crack bandwidth, can be highly affected by the geometry of the elements, whereby differences in results may occur.

The outline of the paper is as follows. In Section 2, a brief summary of the experimental tests by Alfano et al. (2012) is provided, including the key geometrical and measured material properties of the RC beams tested. In Section 3, a description of the FE models developed is given, with detailed explanation of the elements and meshes, loads and boundary conditions and the material models used. The numerical results are compared with the experimental values obtained by Alfano et al. (2012) in Section 4, and are extensively discussed to provide insight into the above–mentioned areas of investigation and novelty. The main conclusions are then summarised in Section 5.

2. Summary of Experimental tests

The performance of the FE models developed in this paper is validated against the experimental tests reported by Alfano et al. (2012). Of particular interest to this work are the two RC control beams, namely beams U2 and U5, which were tested under four–point bending. The beams, which vary in length and cross–section, have the geometrical properties reported in Table 1 (seeFigure 1. Figure 1 for details on the notation).

Table 1. Geometrical properties of the two control beam tested by Alfano et al. (2012)

Beams	*L1* mm	*L2* mm	*b* mm	*h* mm	*c* mm	*d* mm
U2	1000	600	150	300	30	130
U5	800	700	150	250	30	125

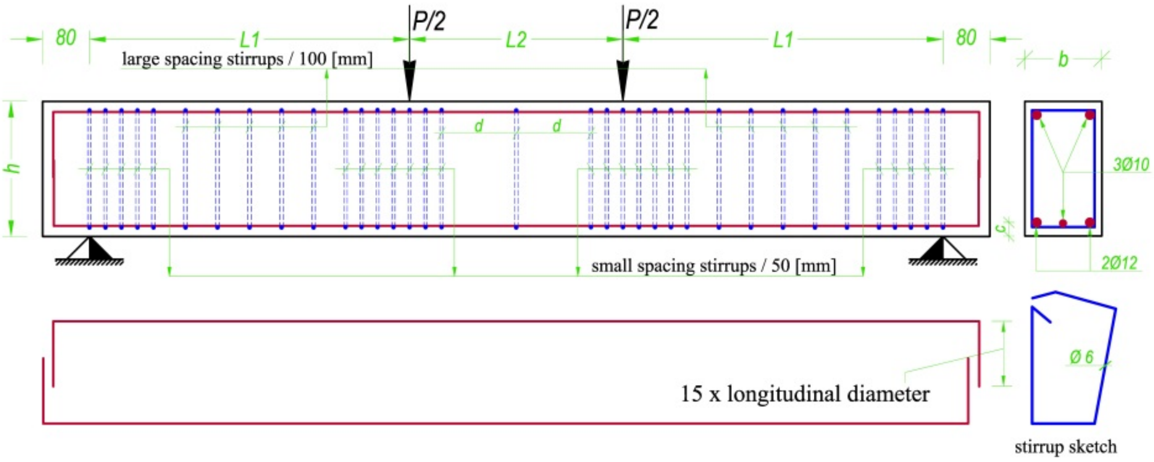

Figure 1. Geometry, reinforcement and loading of the tested beams

The concrete used to cast the two control beams was a mixture of basaltic sand, 10–mm aggregates and cement, with a 0.79 water/cement ratio. Six cubic specimens, 150 mm in size, were tested to determine the concrete compressive strength, whereas the tensile strength was determined by performing Brazilian tests on five concrete cylinders, 150 mm in diameter and 300 mm in length. Furthermore, tests on three cylinders, 150 mm in diameter and 375 mm in length, were performed to determine the Young's modulus of concrete. As for the steel rebars, monotonic tensile tests were performed on steel rebar specimens to determine the yield stress, which confirmed the value of the Young's modulus as provided by the manufacturer. The average material properties for the concrete, steel rebars and stirrups are given in Table 2.

Table 2. Average material properties of concrete and steel bars Alfano et al. (2012)

	Concrete	Steel bars and stirrups
Density kg/m^3	2400	7820
Poisson ratio	0.15	0.30
Young's modulus GPa	26	205
Yield stress MPa	–	380
Cubic compressive strength MPa	19.39	–
Tensile strength MPa	2.00	–

The tested RC beams were loaded by means of one hydraulic actuator and a loading beam in a displacement–controlled mode. Two transducers, which were placed in the mid–span on the beam soffit, symmetrically with respect to the vertical plane through the beam's axis, were used to record the mid–span deflection. The experimental loading history, whose schematic representation is depicted in Figure 2Figure 2. , consisted of:

- Branch OA: loading up to a force, F_{cr}, higher than that corresponding to the cracking bending moment at the beam mid–span;
- Branch AB: unloading to zero;
- Branch BC: reloading up to F_{cr}, and
- Branch CD: where the beam was continued to be loaded up to failure.

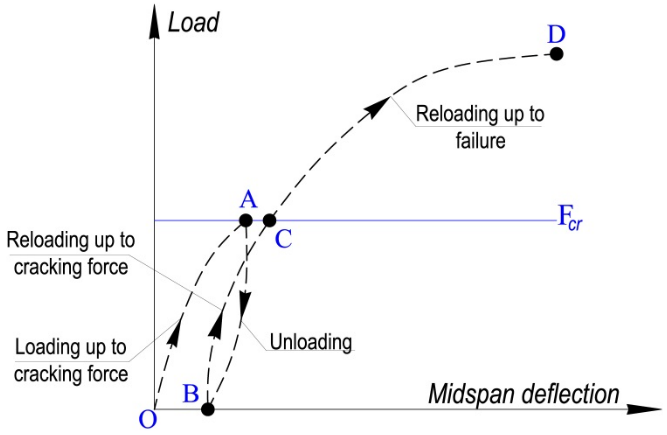

Figure 2. Schematic representation of the loading history: load versus mid–span deflection

3. Nonlinear Finite–Element Modelling

3-1. General

The experimental tests described in the previous section can be numerically modelled using nonlinear FE implicit procedures. However, the use of an implicit procedure to solve problems involving cracking and damage may not be always efficient as convergence difficulties are often encountered, whereas a dynamic explicit (DEXP) analysis can be more efficient to model complex nonlinear material behaviour involving damage and large deformations. Convergence in this context refers to the ability of the iterative algorithm (the most widely used being the Newton–Raphson method) to achieve equilibrium, at the end of a load increment, between external and internal forces, within a predefined numerical tolerance. The salient feature of the DEXP method is that the global tangent stiffness matrix, required otherwise in implicit methods, is no longer formed. Hence, iterations and tolerances are not required because the state of the model is advanced explicitly, that is – the state at the end of the increment is merely based on the displacements, velocities and accelerations at the beginning of the increment. Accurate and stable results can only be obtained with quite small time increments. On the other hand and due to the small time increments, simulations typically require thousands of increments, which are inexpensive because solving simultaneous equations is not required in the DEXP method. Instead, the computational cost lies in the element calculations to determine the elements' internal forces acting on the nodes. Furthermore, a quasi–static solution can be also obtained with the DEXP procedure if the load is applied slowly enough throughout the simulation. Therefore, in the present study, dynamic explicit FE analyses were conducted using the general–purpose FE program ABAQUS.

3-2. Finite–Element Geometry and Mesh

The symmetry of the four–point bending test geometries was exploited by modelling only one–quarter of the full beams.

Structured and unstructured meshes were used to model the concrete. The explicit solver in ABAQUS, denoted 'ABAQUS/Explicit' (Dassault Systèmes 2014b), offers only the use of first–order hexahedral elements for structured meshes, whereas first– and second–order tetrahedral elements can be used for an unstructured mesh. To this end, for structured meshes, 3D 8–noded hexahedral (brick) elements either with reduced integration (C3D8R) or with incompatible modes (C3D8I) were used. The latter elements use, in addition to the standard displacement degrees of freedom, internally incompatible deformation modes, which prevent the behaviour of conventional 8–noded elements from being too stiff in bending by eliminating the shear locking with a small increase in the computational cost (Dassault Systèmes 2014b). For unstructured meshes, either 3D 4–noded linear tetrahedral (C3D4) or 3D 10–noded modified quadratic tetrahedral (C3D10M) elements were used.

3D linear truss (T3D2) elements, 3D linear beam (B31) elements or 3D quadratic beam (B32) elements were used to model the steel rebars. The implementation of these elements in the FE model is related to the mesh being used for the concrete. For example, T3D2 elements were used with structured meshes, B31 elements were used with first–order structured and unstructured meshes, and B32 elements were only used with second–order unstructured meshes. On the other hand, the stirrups were modelled using T3D2 and/or B31 elements (i.e. T3D2 elements were used when the steel rebars were modelled using T3D2 elements, otherwise B31 elements were used). The steel rebars and stirrups are 'embedded' in the concrete geometry, so that their translational degrees of freedom are constrained to the corresponding concrete degrees of freedom (Dassault Systèmes 2014b).

To investigate the influence of the density of the FE mesh on the cracking behaviour of the concrete and its ultimate–load carrying capacity, computations were performed using three different element sizes.

3-3. Boundary Conditions and Load Application

The beam end–supports, which were provided experimentally by two steel rollers, were modelled in a simplified way to avoid stress concentrations entailed by the application of displacement boundary conditions on a line. As such, a 30 mm wide surface (see Figure 3) was constrained to a reference point lying on this surface with a rigid body motion. The vertical displacement only of the reference point (i.e. in the Y −direction in Figure 3) was blocked and all other rotational degrees of freedom were allowed. Symmetry boundary conditions were applied on the symmetric planes of the four–point bending test, as shown in Figure 3.

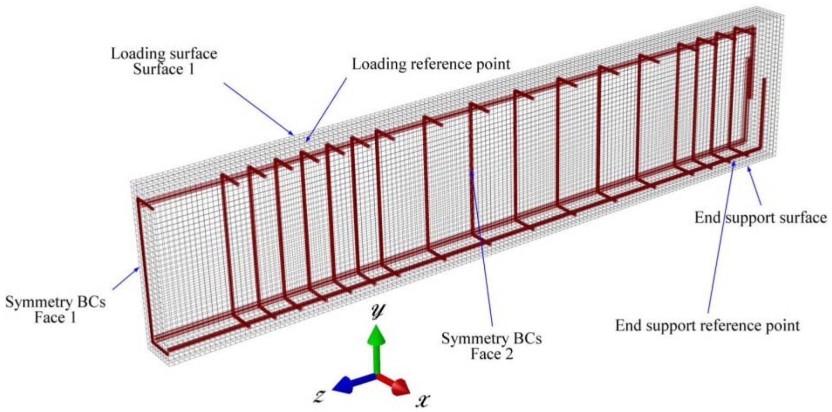

Figure 3. Finite element model and boundary conditions

Likewise, the steel roller of the coupling beam, used to load the RC beam, were also modelled with a 20 mm wide surface, designated as Surface 1 in Figure 3, constrained to a reference point lying on the same surface. Displacement–controlled was used, by prescribing the vertical displacement of this reference point according with the scheme of Figure 2, the other degrees of freedom being free. The displacement–controlled strategy was used to load the FE model.

To ensure a quasi–static solution is obtained with the dynamic explicit procedure implemented in this study, the displacement was applied smoothly and slowly to eliminate any significant change in the acceleration from one increment to the other. This further ensures the smoothness of the changes in the velocity and displacement. To this end, a 'smooth–step' amplitude was used to prescribe the displacement to the model. Accordingly, five data points, $(t_i, A_i)\ i\colon 0 \rightarrow 4$, which define the variation of the amplitude value with time, were used to define the amplitude, a, whose expression is as follows (Dassault Systèmes 2014b):

$$\begin{gathered} a(\xi) = A_i + (A_{i+1} - A_i)\xi^3(10 - 15\xi + 6\xi^2) \\ \xi = \frac{(t - t_i)}{(t_{i+1} - t_i)} \quad \text{for} \quad t_i \leq t \leq t_{i+1} \end{gathered} \tag{1}$$

The salient feature of this amplitude function is that its first and second derivatives are zeros at t_i and t_{i+1}, ensuring that the prescribed displacement is smoothly ramped up using a smooth curve, as shown in Figure 4.

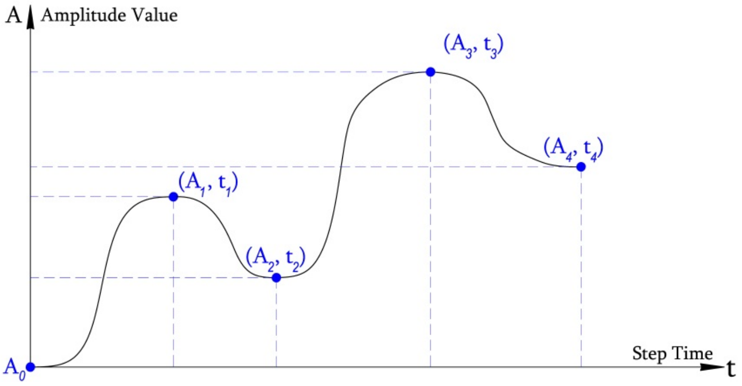

Figure 4. Schematic smooth step amplitude definition (Dassault Systèmes 2014b)

3-4. Dynamic Explicit Solution Scheme

The equation of motion and its related initial conditions for a static structural problem when treated as a dynamic one can be expressed as follows (Huebner, Dewhirst et al. 2008):

$$\boldsymbol{M\ddot{u}} + \boldsymbol{C\dot{u}} + \boldsymbol{Ku} = \boldsymbol{P(t)}$$

$$\boldsymbol{u}(t=0) = \boldsymbol{u_0} \qquad \dot{\boldsymbol{u}} = \left.\frac{\partial \boldsymbol{u}}{\partial t}\right|_{t=0} = \boldsymbol{v_0} \qquad \ddot{\boldsymbol{u}} = \left.\frac{\partial^2 \boldsymbol{u}}{\partial^2 t}\right|_{t=0} = \boldsymbol{\alpha_0} \tag{2}$$

where $\boldsymbol{M}$, $\boldsymbol{C}$ and $\boldsymbol{K}$ are the mass, damping and stiffness matrices, respectively. $\boldsymbol{u_0}$, $\boldsymbol{v_0}$ and $\boldsymbol{\alpha_0}$ are the displacement, velocity and acceleration, respectively and $\boldsymbol{P(t)}$ is the nodal forces vector. Eq. (2) is a second–order differential equation, which can be effectively solved using the central–difference method (CDM). The latter technique being a preferable choice in structural dynamics.

The simulations conducted in this study were highly nonlinear involving significant damage and strain localisation. These phenomena are inherently challenging as they continuously change the highest frequency of the model, inducing a change in the stability limit, $\Delta t_{min} \le {}^{L^e}/_{c_d}$, where L^e is the element characteristic length and c_d is the speed of the dilatational wave. For instance, a reduction in Δt_{min} may always be associated with damage (i.e. element distortion). Therefore, to ensure the stability of the predicted solution and maximise its accuracy, ABAQUS/Explicit solver was allowed to automatically adjust the time incrementation. However, the estimation of Δt_{min} was specified based on an 'element–by–element' style, whereby the contribution of the current speed of the dilatational wave, c_d, in each FE determined Δt_{min}. This yields accurate estimation of Δt_{min} as opposed to that estimated based on the maximum frequency of the entire model. Despite being conservative, the element–by–

element stable time estimate maintains a smaller stability limit compared to that of the default adaptive 'global' estimate employed in the Explicit solver.

All simulations presented in this study were run in a parallel scenario, utilising the computational resources of 12 central processing units (CPUs) (2.70 GHz (up to 3.50 GHz) Intel® Xeon E5–2697 v2; 12 cores/24 threads), and one graphic processing unit (GPU) (8GB Nvidia® Quadro K5100M; 1536 CUDA @ 771 MHz). It is worth emphasising here that these simulations were performed using the 'double precision' executable, which typically results in a significant increase in increments on top of 20–30% increase in the computational cost in comparison with running the 'single precision' executable. The latter was opted out as it yielded a significant noise in the load–deflection predictions due to the presence of a combination of boundary conditions and rigid body constraints. Instead, the double precision executable, in such case, better estimates the work done by the reaction forces and moments, and therefore, accurately computes the energy induced by the external work, resulting in ultimately a stable solution.

3-5. Material Models

3-5-1. Concrete

The concrete nonlinearity under compression can be modelled within the framework of either plasticity or damage, or both (Yu, Teng et al. 2010b). Plasticity is generally characterised by the formation of unrecoverable deformation once all loads have been removed, whereas damage is characterised by the reduction of elastic stiffness. The concrete damaged–plasticity (CDP) model was employed to model the behaviour of the two control beams, U2 and U5.

The CDP model, widely used for concrete, is a continuum, smeared–crack model combining damage and plasticity, which is implemented in ABAQUS (Dassault Systèmes 2014b) and is based on the work by Lubliner et al. (1989) and Lee and Fenves (1998). While these references contain detailed information on the models, some key equations are included herein in order to explain the input parameters used, their meaning and how they were determined.

The model assumes that the so–called compressive crushing and tensile cracking are the main two failure mechanisms of the material. The response of the CDP model under uniaxial tensile loading is characterised by a linear–elastic stress–strain relationship up to the value of the failure stress. At such a stress, micro–cracks in the concrete material start forming. The progressive coalescence of micro–cracks into macro–cracks and their subsequent openings are then captured using a softening stress–strain relationship. This latter relationship models the tensile cracking behaviour of concrete and can be defined by the so–called ‘tension softening’ by means of either a post–failure stress–strain relation or a fracture energy cracking criterion.

Under uniaxial compressive loading, the CDP model behaves linearly until the value of the initial yield is reached, followed by a stress hardening and strain softening beyond the ultimate stress.

In the CDP model, the following non–associated plastic flow rule is used:

$$\dot{\boldsymbol{\varepsilon}}_p = \dot{\lambda}\frac{\partial G}{\partial \boldsymbol{\sigma}} \tag{3}$$

where $\boldsymbol{\sigma}$ and $\dot{\boldsymbol{\varepsilon}}_p$ denote the stress and plastic strain rate tensors, respectively, $\dot{\lambda}$ is a plastic multiplier, and G is the Drucker–Prager function is used in the model:

$$G = \sqrt{(\epsilon\sigma_{t0}\tan\psi)^2 + \overline{q}^2} - \overline{p}\tan\psi \tag{4}$$

In the above equation, $\overline{p}$ and $\overline{q}$ are the hydrostatic stress and the von Mises equivalent stress, respectively:

$$\overline{p} = -\tfrac{1}{3}\,\mathrm{tr}(\boldsymbol{\sigma}) \qquad \overline{q} = \sqrt{\tfrac{3}{2}}\,\|\mathrm{dev}(\boldsymbol{\sigma})\|; \tag{5}$$

ψ is the dilation angle measured in the $\overline{p} - \overline{q}$ plane at high confining pressure; ϵ is the eccentricity, a parameter that defines the rate at which the function approaches the asymptote; σ_{t0} is the uniaxial tensile stress at failure. For σ_{t0} the value measured by Alfano et al. (2012) and reported in Table 2 was used. For the eccentricity ϵ, which defines the rate at which Eq. (4) approaches the asymptote, the default value of 0.1 was used because it results in the same dilation angle over a wide range of confining pressure stress states. A sensitivity analysis of ϵ not presented here was conducted using $\epsilon = 0.2$ and $\epsilon = 0.3$ and it showed that this parameter had no effect on the load–deflection response of the two beams presented in this work. A value of ϵ that is significantly less than 0.1 is not recommended as it may lead to convergence issues (Dassault Systèmes 2014b). As for the dilation angle ψ, after conducting a sensitivity analysis reported below in Section 4-1-1, the value 40° was used.

To account for the different evolution of strength under compression and tension, the CDP model uses the yield function of Lubliner et al. (1989), with the modifications suggested by Lee and Fenves (1998). The yield surfaces in the plane stress and deviatoric plane conditions are depicted in Figure 5(a) and Figure 5(b), respectively. The yield function defined by

Lubliner et al. (1989) can be expressed in terms of the effective stress as follows (Dassault Systèmes 2014b):

$$F = \frac{1}{1-\alpha}\left[\bar{q} - 3\alpha\bar{p} + \beta\left(\tilde{\varepsilon}_t^{pl}, \tilde{\varepsilon}_c^{pl}\right)\langle\hat{\bar{\sigma}}_{max}\rangle - \gamma\langle-\hat{\bar{\sigma}}_{max}\rangle\right] - \bar{\sigma}_c\left(\tilde{\varepsilon}_c^{pl}\right) \tag{6}$$

where

$$\alpha = \frac{(\sigma_{b0}/\sigma_{c0}) - 1}{2(\sigma_{b0}/\sigma_{c0}) - 1};\ \ 0 \le \alpha \le 0.5 \tag{7}$$

$\hat{\bar{\sigma}}_{max}$ is the maximum principal effective stress, σ_{b0}/σ_{c0} is the ratio of initial equi–biaxial compressive yield stress to initial uniaxial compressive yield stress. σ_{b0}/σ_{c0} was set to the default value of 1.16 in the conducted simulations, which is the maximum of the range of experimentally found values reported by Lubliner et al. (1989), the minimum being 1.10. The effect of using different values of σ_{b0}/σ_{c0} (e.g. 1.0, 1.3 and 1.4) on the numerical load–deflection curve was investigated. Numerical results not presented here showed that this parameter had negligible influence on the predicted load–deflection response.

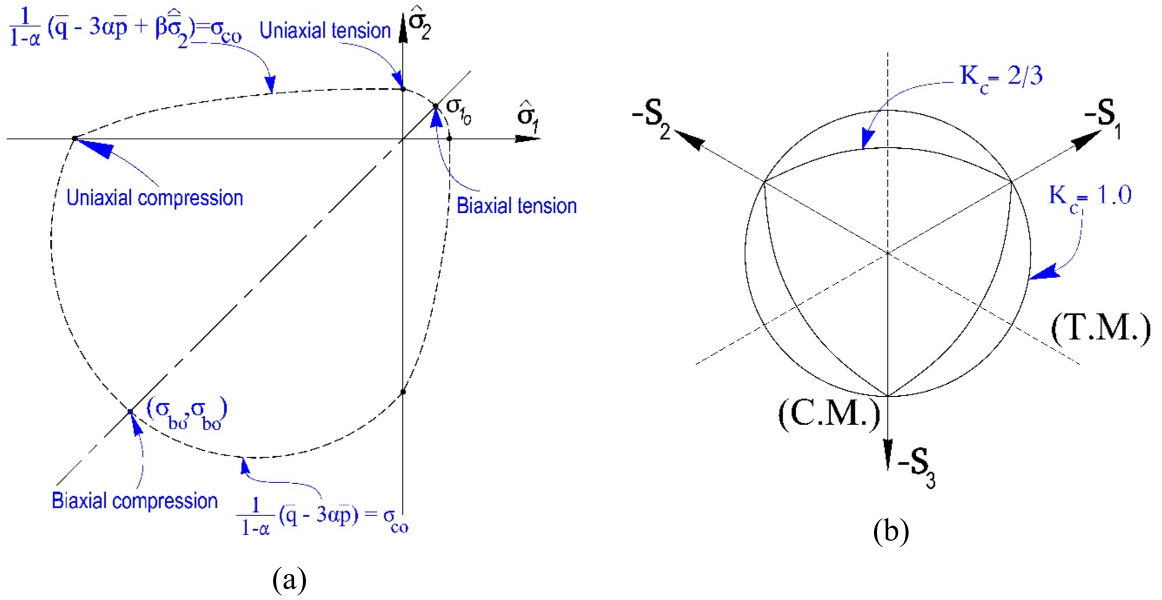

(a)

(b)

Figure 5. Concrete yield surface in (a) plane stress and (b) deviatoric plane

In Eq.(6), β and γ are defined as follows:

$$\beta = \frac{\bar{\sigma}_c\left(\tilde{\varepsilon}_c^{pl}\right)}{\bar{\sigma}_t\left(\tilde{\varepsilon}_t^{pl}\right)}(1-\alpha) - (1+\alpha);\ \ \gamma = \frac{3(1-K_c)}{2K_c - 1} \tag{8}$$

where $\bar{\sigma}_c\left(\tilde{\varepsilon}_c^{pl}\right)$ and $\bar{\sigma}_t\left(\tilde{\varepsilon}_t^{pl}\right)$ are cohesion values in tension and compression, assumed to depend on the compressive and tensile equivalent plastic strains, $\tilde{\varepsilon}_c^{pl}$ and $\tilde{\varepsilon}_t^{pl}$, respectively. Note that β

was assumed to be constant by Lubliner et al. (1989), while the expression given in (7) was proposed by Lee and Fenves (1998), to account for the case of cyclic loading, which is of interest in this paper. Parameter $K_c = q_{(TM)}/q_{(CM)}$, where $q_{(TM)}$ and $q_{(CM)}$ are the von Mises equivalent stresses on the tensile meridian (TM) and on the compressive meridian (CM), shown in Figure 5(b), at any value of the hydrostatic stress (Lubliner et al., 1989). In the simulations presented in this paper, K_c was set to the default value of $2/3$, which is in line with what suggested by Lubliner et al. (1989).

- *Compressive Behaviour*

The uniaxial stress–strain behaviour of concrete was determined in accordance with the Eurocode 2 (2004), whose schematic representation is shown in Figure 6, and has the following expression:

$$\frac{\sigma_c}{f_{cm}} = \frac{k\eta - \eta^2}{1 + (k - 2)\eta} \tag{9}$$

where σ_c is the concrete compressive stress, f_{cm} is the mean value of concrete cylinder compressive strength. Furthermore, $\eta = \varepsilon_c/\varepsilon_{c_1}$, where ε_c is the concrete compressive strain and $\varepsilon_{c_1} = 0.7f_{cm}^{0.31}$ is the concrete compressive strain at the peak stress, f_{cm} being the average cylindrical compressive strength expressed in MPa, while $k = 1.05E_{cm}|\varepsilon_{c_1}|/f_{cm}$, with E_{cm} being the average Young's modulus of concrete in MPa. For E_{cm}, the value in Table 2 was used, whereas f_{cm} was estimated in accordance with BS EN 206–1 (2000) to be 20% less than the cubic compressive strength, $f_{cm,cube}$, reported in Table 2.

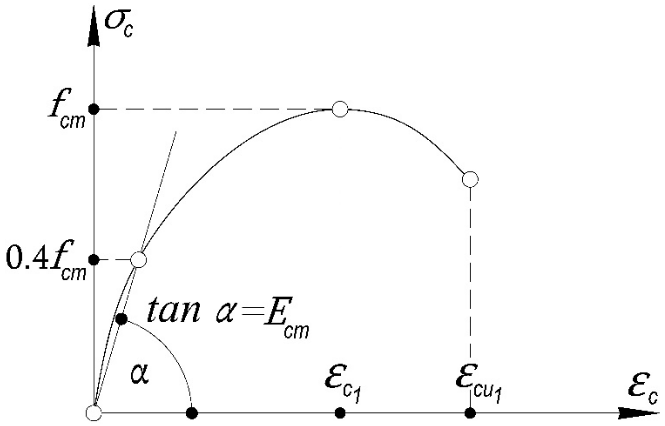

Figure 6. Schematic representation of the unaxial compressive stress–strain relation for the structural analysis of concrete (British Standard Institution 2004)

Eq. (9) is valid for $0 < |\varepsilon_c| < |\varepsilon_{cu_1}|$, where $|\varepsilon_{cu_1}|$ is the nominal ultimate strain. As per the Eurocode (2004), ε_{cu_1} can be taken as 0.0035 for concrete compressive cylindrical strength of $12 - 50$ MPa. Otherwise, the ultimate compressive strain for concrete with a greater compressive strength can be estimated using the relation $\varepsilon_{cu_1} = 2.8 + 27[0.01(98 - f_{cm})]^4$ (where f_{cm} is expressed in MPa).

Figure 7(a) shows the uniaxial stress–strain curve used to define the compressive behaviour of concrete.

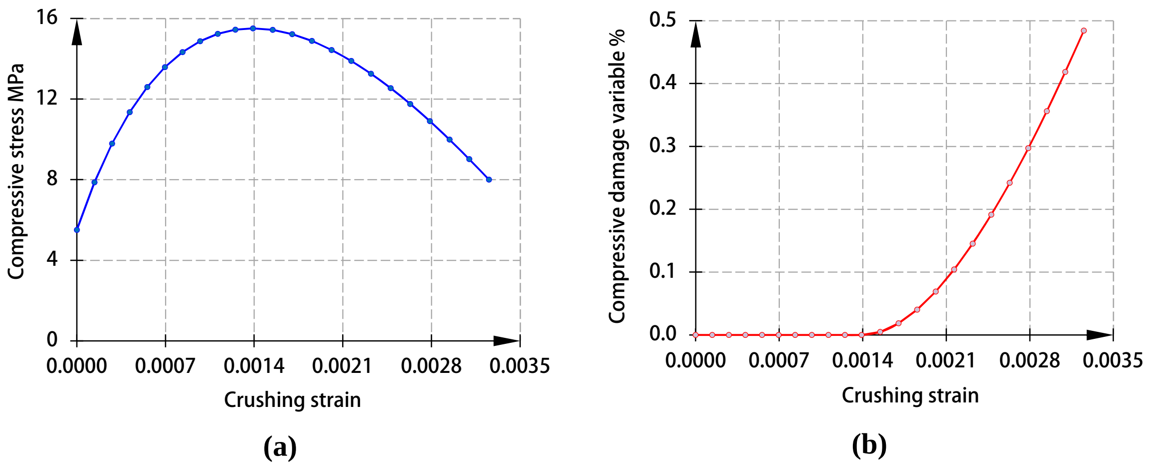

(a) **(b)**

Figure 7. Concrete compressive behaviour: (a) Stress–strain curve, (b) Compressive damage evolution

- *Tensile Behaviour*

The concrete behaviour under uniaxial tension can be modelled by means of the so–called 'tension softening' behaviour, also known as 'tension stiffening', which models the stress transfer between the reinforcement and concrete. This can be done by providing the stress–relative displacement curve, which would characterise the cracking behaviour of concrete if a discrete–crack approach was used. The area under such curve represents the fracture energy (Hillerborg, Modéer et al. 1976). Different types of relationships can be used, as depicted in Figure 8. The simplest approach is to assume a linear approximation to define the tensile cracking behaviour. Such approximation yields reasonably accurate results but the concrete response tends to be too stiff. Instead, a smooth tension stiffening function is ideally recommended, such as a bi–linear approximation (Hillerborg 1985, CEB-FIP 1993) or an exponential expression (Cornelissen, Hordijk et al. 1986, Hordijk 1991) to define the descending part of the stress–displacement curve. The former is an acceptable formulation that agrees well with test data, although the location of the kink point has been predominantly debated in the literature. The stress ratio at this point has been suggested to be between 0.15 and 0.33 (Park, Paulino et al. 2008). Hillerborg (1985) proposed the coordinates of the kink point at $(0.15\, f_t, 0.8\, G_F/f_t)$, whereas these coordinates were suggested by CEB-FIP (1993) to be $(0.33 f_t, 2\, G_F/f_t - 0.15 w_{cr})$, where $w_{cr} = \alpha_F\, G_F/f_t$, G_F and α_F being the total fracture energy and a dimensionless coefficient that is dependable on the aggregate size, respectively. The latter reported by Alfano et al. (2012) as 10 mm, which corresponds to α_F value of 7.75.

It can be noted, therefore, that the tail of the bi–linear approximation of CEB-FIP (1993) is twice as long as that of Hillerborg (1985). However, the crack–opening displacement at the kink point will be identical for both bi–linear curves when substituting the corresponding values of G_F, being calculated later in this Section, and w_{cr}.

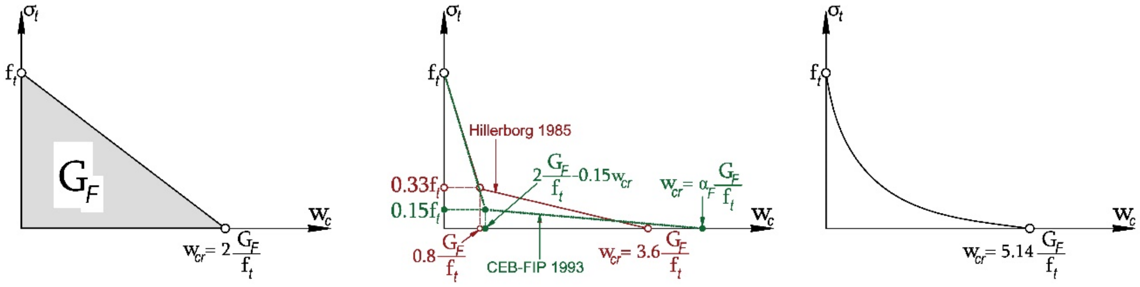

(i) Linear function (ii) Bi–linear function (iii) Exponential function

Figure 8. Linear (Dassault Systèmes 2014b), Bi–linear (Hillerborg 1985, CEB-FIP 1993) and exponential (Cornelissen, Hordijk et al. 1986) tension–softening models

In their study, Roesler, Paulino et al. (2007) concluded that the predicted post–peak load behaviour is influenced by G_F and the stress ratio at the kink point, whereas the tensile strength and the stiffness of the stress–displacement relationship, being fully characterised by G_f, control the predicted peak–load. These conclusions were also confirmed by Bažant and Becq-Giraudon (2002). It is worth emphasising here that G_f and G_F are two different material characteristics, which determine the slope (i.e. stiffness) of the stress–displacement relationship and its tail, respectively. The two fracture energies are approximately related by the relation $G_f = 0.4 G_F$ (Planas, Elices et al. 1992).

The present study aims at investigating the predicted load–deflection response of two RC beams, particularly, the behaviour in the post–peak region, the latter being dependable on the tail of the tension stiffening law employed in the model. The numerical results predicted using the bi–linear and exponential tension stiffening laws in Figure 8 and presented in Section 4-1-2, show that the tail of the tension stiffening law has no effect on the predicted post–peak load–

deflection response providing that the same G_F value is used. The tail of the exponential law is 1.5 longer than that of Hillerborg (1985) bi–linear law; yet, the predicted response remains unaffected. To this end, the numerical response predicted with either of the bi–linear curves depicted in Figure 8 is expected to be similar. Hence, the bi–linear curve of Hillerborg (1985) is chosen due to its wide use in the computational modelling of concrete.

In this study, the three types of the stress–cracking displacement tension–softening laws, linear, bi–linear and exponential were compared. These responses are plotted in Figure 9(a).

The exponential law of Cornelissen et al. (1986) has the following expression:

$$\frac{\sigma_t}{f_t} = \left[1 + \left(c_1 \frac{w_t}{w_{cr}}\right)^3\right] \exp\left(-c_2 \frac{w_t}{w_{cr}}\right) - \frac{w_t}{w_{cr}}(1 + c_1^3)\exp(-c_2)$$
$$w_{cr} = 5.14 \frac{G_F}{f_t} \tag{10}$$

where σ_t is the tensile stress normal to the crack direction, f_t is the concrete uniaxial tensile strength, w_t is the crack–opening displacement, w_{cr} is the crack–opening displacement at the complete release of stress or fracture energy, c_1 and c_2 are material constants taken as 3.00 and 6.93, repectively. G_F is the total fracture energy of concrete required to create a stress–free crack over unit surface.

Alfano et al. (2012) reported the concrete tensile strength as a splitting tensile strength. The CDP model, however, requires the uniaxial tensile strength as an input. To this end, the Eurocode 2’s (2004) relation $f_{ct} = 0.9 f_{ct,sp}$ was used to convert the splitting tensile strength into a uniaxial one.

G_F in Eq. (10) can be estimated using the expression $G_F = G_{F_0}(0.1 f_{cm})^{0.7}$ in accordance with the CEB–FIB (1993), where G_{F_o} is the base value of the fracture energy, which is dependable on the maximum size of the aggregate being used in the concrete mixture and f_{cm} is expressed in MPa. The value of G_{F_o}corresponding to a 10 mm maximum aggregate size, as reported earlier in this paper, equals to $0.026\ \mathrm{N/mm}$.

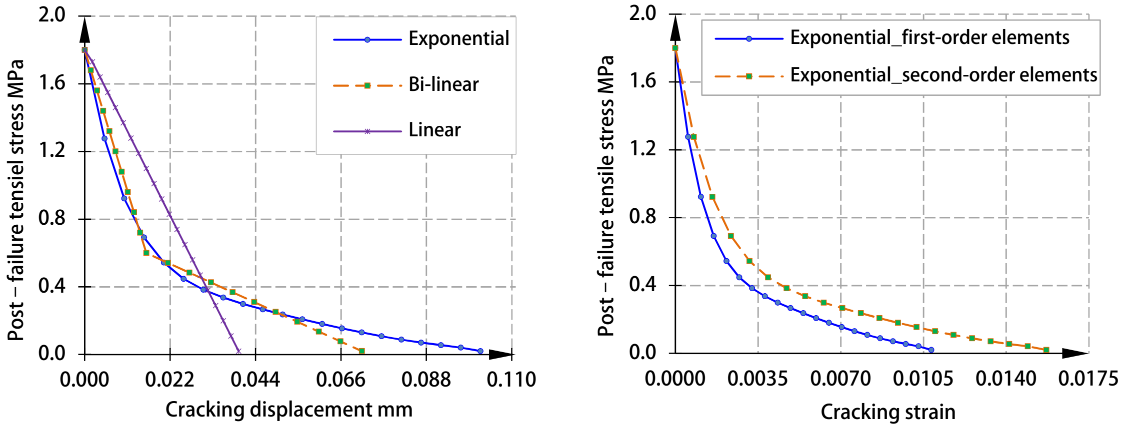

(a) **(b)**

Figure 9. Post–failure tensile behaviour of concrete (a) Stress versus cracking displacement curves, and (b) Stress versus cracking strain

The stress versus crack–opening displacement curves, shown in Figure 9(a), can be converted into a stress versus strain curves using the crack band model. The crack band width, h_c, is defined in ABAQUS as the characteristic crack length, l_{ch}, of an element, which is based on the element geometry and formulation. For instance, for a first–order element, the characteristic crack length is a typical length across the element, whereas it is half of the same typical length for a second–order element. In the present work, l_{ch} was taken as e and $e/2$, where e is the side length of the element, for first– and second–order elements, respectively. Based on the preceding definition of the characteristic length, the exponential stress versus displacement curve was converted into tensile stress versus cracking strain curves as shown in Figure 9(b).

In practical terms, when post–failure stress–strain relationships are used, a single value of l_{ch} must be determined before the analysis based on the average sizes of the entire finite–elements. This was done for all of the analyses, which are reported below.

- *Damage Evolution*

As depicted in Figure 10, which illustrates the tensile and compressive stress–strain curves of concrete, the unloading of the concrete specimen from any point on the softening branch of the curve weakens the initial elastic stiffness, E_c (i.e. damage or degradation appears in the material response). In the CDP model, two damage variables, namely d_c and d_t, are used to characterise the degradation of the elastic stiffness. The values of the compressive damage variable, d_c, and the tensile damage variable, d_t, can range from zero, representing an undamaged material, to one, representing a complete loss of strength. The former variable is assumed to be a function of the compressive plastic strain (i.e. $d_c = d_c(\tilde{\varepsilon}_c^{pl});\ \ 0 \leq d_c \leq 1$), whereas the latter is assumed to be a function of either the tensile plastic strain (i.e. $d_t = d_t(\tilde{\varepsilon}_t^{pl});\ \ 0 \leq d_t \leq 1$), or the tensile plastic displacement (i.e. $d_t = d_t(\tilde{u}_t^{pl});\ \ 0 \leq d_t \leq 1$).

If the concrete specimen is unloaded under uniaxial tension, one of two possible scenarios can arise depending on whether the concrete stiffness has been lost or not after tensile cracking. If this stiffness has not been lost, the unloading path remains parallel to the initial loading path and the corresponding elastic strain will be $\varepsilon_t^{el} = \sigma_t/E_c$, otherwise, the slope of the unloading path will be reduced to $(1 - d_t)E_c$ and the corresponding elastic strain becomes $\varepsilon_{t,d}^{el} = \sigma_t/[(1 - d_t)E_c]$. A similar response is observed if the concrete specimen is unloaded under uniaxial compression. If the compressive stiffness remains intact after compressive crushing, the slope of the unloading path remains equal to that of the initial loading and the corresponding elastic strain is $\varepsilon_c^{el} = \sigma_c/E_c$, otherwise, the compressive stiffness of the unloading path is reduced to $(1 - d_c)E_c$, resulting in a corresponding elastic strain $\varepsilon_{c,d}^{el} = \sigma_c/[(1 - d_c)E_c]$.

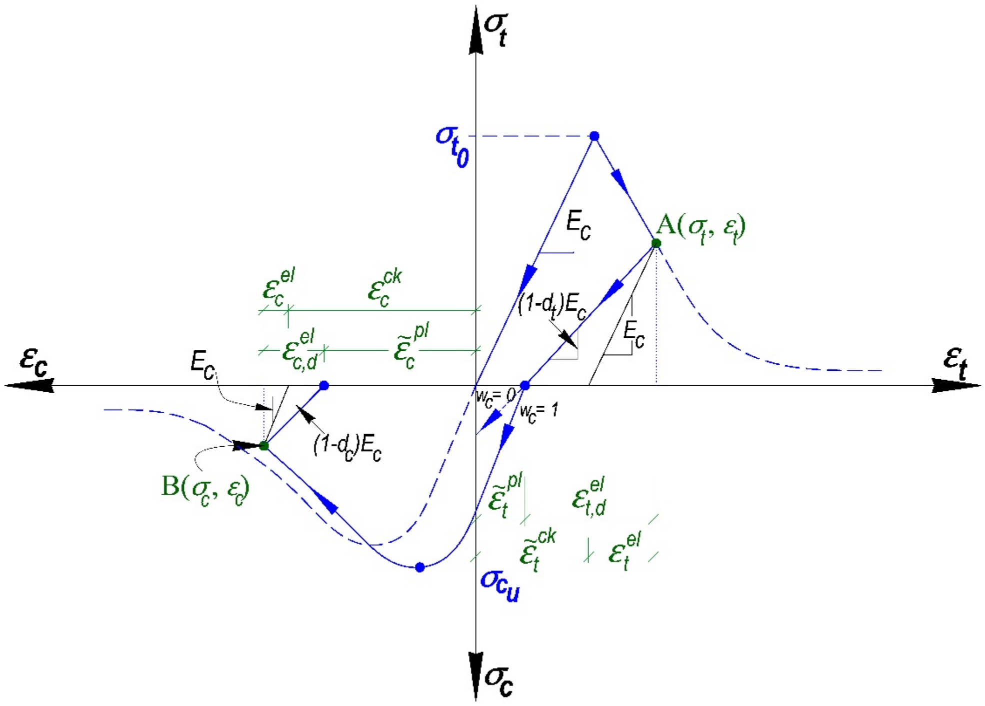

Figure 10. Definition of tensile and compressive damage (reproduced from Dassault Systèmes (2014b))

In the proposed FE models, two user–defined curves were introduced to account for the compressive and tensile damage, as the unloading data were not reported experimentally. As per the CDP model, the compressive damage variable is defined as a tabular function of the (inelastic) crushing strain, $\tilde{\varepsilon}_c^{in}$. The latter is defined as:

$$\tilde{\varepsilon}_c^{in} = \varepsilon_c - \varepsilon_{c_0}^{el} \text{, where: } \varepsilon_{c_0}^{el} = \frac{\sigma_c}{E_c} \tag{11}$$

As shown in Figure 10, the equivalent plastic strain for crushed concrete is:

$$\tilde{\varepsilon}_c^{pl} = \varepsilon_c - \varepsilon_{c,d}^{el} \text{, where: } \varepsilon_{c,d}^{el} = \frac{\sigma_c}{(1-d_c)E_c} \tag{12}$$

From Eq. (11), $\varepsilon_c = \tilde{\varepsilon}_c^{in} + \varepsilon_{c_0}^{el}$. Substituting in Eq. (12) yields:

$$\tilde{\varepsilon}_c^{pl} = \tilde{\varepsilon}_c^{in} + \varepsilon_{c_0}^{el} - \frac{\sigma_c}{(1-d_c)E_c} = \tilde{\varepsilon}_c^{in} - \frac{\sigma_c}{E_c}\left(\frac{1}{1-d_c} - 1\right) = \tilde{\varepsilon}_c^{in} - \frac{d_c}{1-d_c}\varepsilon_{c_0}^{el} \tag{13}$$

The compressive damage variable can be computed using the following relation:

$$d_c = 1 - \frac{\sigma_c}{f_{cm}} \tag{14}$$

It is assumed that $\tilde{\varepsilon}_c^{pl} = 0$ for $\sigma_c \leq \sigma_{c_u}$. Following the preceding definition of the compressive damage of concrete, the damage evolution is directly determined by the compressive stress–strain relationship (e.g. Eq. (9)). The $\tilde{\varepsilon}_c^{in} - d_c$ curve defined using this method is shown in Figure 7(b).

Similarly, the tensile damage variable can be defined as a tabular function of either the crack–opening displacement, $\tilde{u}_t^{ck}$, or the cracking strain, $\tilde{\varepsilon}_t^{in}$. Either way, the tensile damage variable can be computed using the relation $d_t = 1 - (\sigma_t/f_t)$. The plastic displacement can be determined using the following relationship:

$$\tilde{u}_t^{pl} = \tilde{u}_t^{ck} - \frac{d_t}{1-d_t}\varepsilon_{t_0}^{el}\text{, where: } \varepsilon_{t_0}^{el} = \frac{\sigma_t}{E_c} \tag{15}$$

Based on the aforementioned definition of the tensile damage, the damage evolution law is directly determined by the tension–softening law being implemented in the FE model (e.g. Figure 9(a)). Figure 11 shows three $\tilde{u}_t^{ck} - d_t$ curves determined using the preceding method.

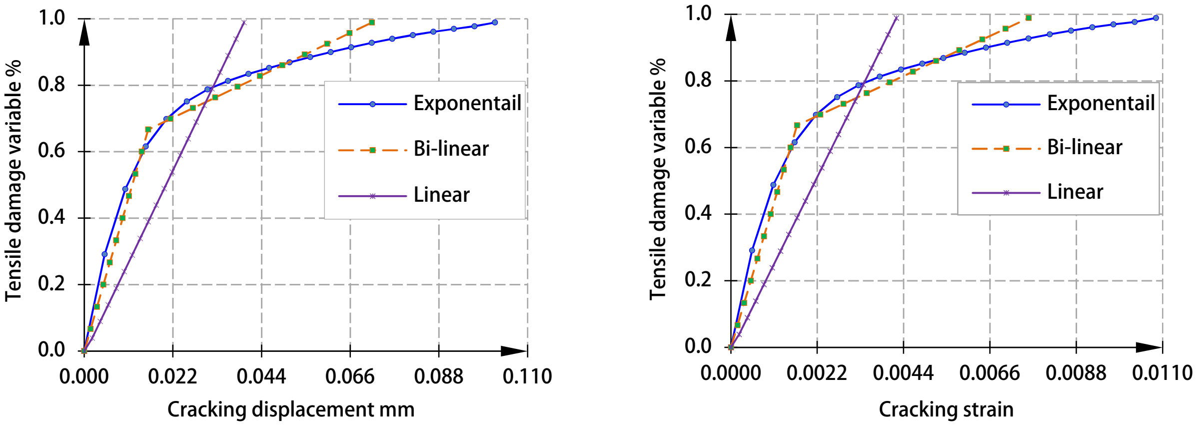

(a) **(b)**

Figure 11. Tensile damage variable versus (a) crack–opening displacement, and (b) cracking strain

The cracking strain is defined in ABAQUS as:

$$\tilde{\varepsilon}_t^{ck} = \varepsilon_t - \varepsilon_{t_0}^{el} \text{ , where: } \varepsilon_{t_0}^{el} = \frac{\sigma_t}{E_c} \tag{16}$$

With reference to Figure 10, the plastic strain for damaged concrete is:

$$\tilde{\varepsilon}_t^{pl} = \varepsilon_t - \varepsilon_{t,d}^{el} \text{ , where: } \varepsilon_{t,d}^{el} = \frac{\sigma_t}{(1-t)E_c} \tag{17}$$

From Eq. (16), $\varepsilon_t = \tilde{\varepsilon}_t^{ck} + \varepsilon_{t_0}^{el}$. Substituting in Eq. (17) yields:

$$\tilde{\varepsilon}_t^{pl} = \tilde{\varepsilon}_t^{ck} + \varepsilon_{t_0}^{el} - \frac{\sigma_t}{(1-d_t)E_c} = \tilde{\varepsilon}_t^{ck} - \frac{\sigma_t}{E_c}\left(\frac{1}{1-d_t} - 1\right) = \tilde{\varepsilon}_t^{ck} - \frac{d_t}{1-d_t}\varepsilon_{c_0}^{el} \tag{18}$$

The post–failure stress–strain relation (e.g. Figure 9(b)), being implemented in the FE model to define the tension–softening, directly determines the damage evolution law in this case. The three corresponding $\tilde{\varepsilon}_t^{ck} - d_t$ curves are depicted in Figure 11.

3-5-2. Steel

The steel of the longitudinal rebars and stirrups were modelled as an elastic–perfectly plastic material. Table 2 shows the material properties for the steel rebars and stirrups. The bond–slip interaction was accounted for because the CDP model captures the damage of the concrete surrounding the steel rebars.

4. Results and Discussion

In the following sub–sections, the numerical results are presented in terms of the load–carrying capacity versus deflection and predicted crack patterns for the two RC control beams, tested by Alfano et al. (2012) and chosen to validate the FE models described in this paper. The effects of (i) the shape of the tension softening curve (i.e. linear, bi–linear and exponential), (ii) the finite–element type used to represent the rebars (e.g. truss or beam elements with linear or nonlinear geometric nonlinearity), (iii) the finite–element type used to represent the concrete (e.g. tetrahedron or hexahedron) and the density of the mesh (coarse, medium or fine) on the structural response of the two RC beams are investigated.

4-1. Load–Deflection Curves

4-1-1. Effects of Dilation Angle

The influence of the size of the dilation angle on the load–deflection response was studied for the two RC beams presented in this work. The analyses were conducted using a fine structured mesh of C3D8I elements, whose edges were of identical lengths of 10 mm. Longitudinal steel rebars and stirrups were modelled using B31 elements. An exponential stress–displacement tension–softening law was employed in these analyses. Four different sizes of the dilation angle of 20°, 30°, 40° and 50°, respectively, were studied. The numerical load–deflection curves are presented in Figure 12(a) for beam U2 and in Figure 12(b) for beam U5.

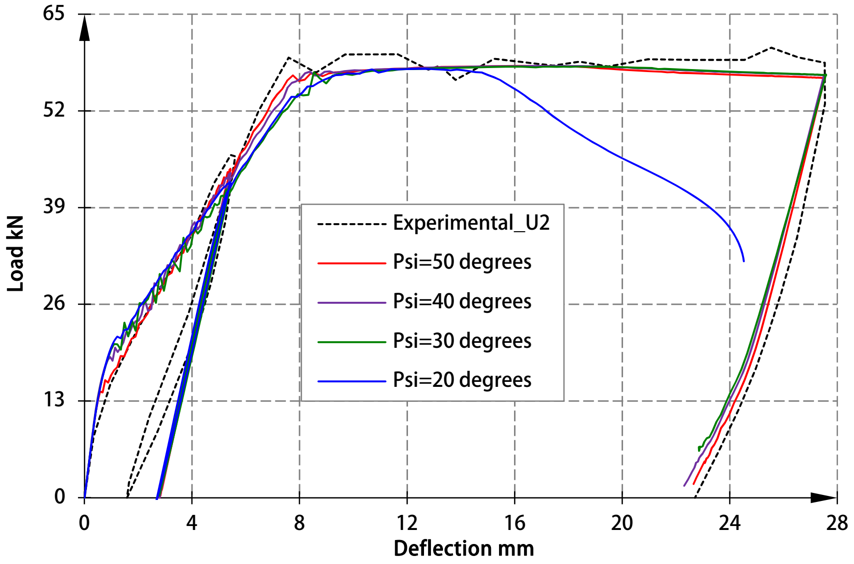

(a)

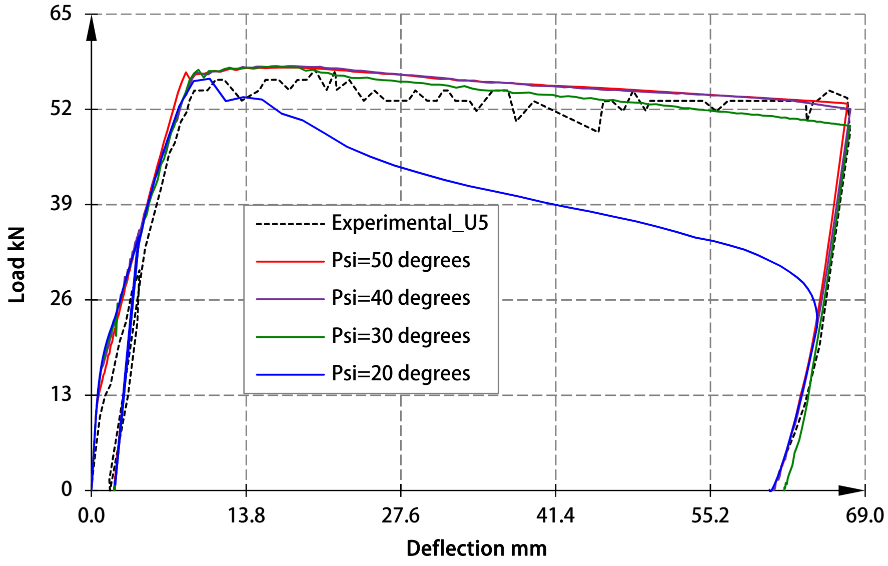

(b)

Figure 12. Effects of dilation angle on the numerical load–deflection curves of (a) beam U2 and (b) beam U5

It can be seen from Figure 12Figure 12. that a small value of the dilation angle (i.e. $= 20^\circ$) results in a significant loss of ductility whilst the differences in the load–deflection response for higher values (e.g. $\psi = 30^\circ, 40^\circ$ and 50°) are rather small. Based on this sensitivity analysis, ψ was set to 40° in all the conducted simulations.

4-1-2. Effects of Tension–Softening Definition

The numerical load–deflection curves, predicted using the tension–softening stress–displacement relations shown in Figure 9(a), are compared in Figure 13(a) against the experimental load–deflection curve of beam U2. In the FE analyses, the concrete was modelled using C3D8I elements and the longitudinal rebars and stirrups were modelled using B31 elements. The predicted cracking loads, residual deflections and ultimate–loads reported in Figure 13(a) show that the numerical cracking loads are slightly under–predicted with differences all between 1 and 4%. The predicted residual deflections upon the first unloading, however, are higher than the experimental value, with differences between 40 and 45%. The ultimate–load is closely predicted with differences all below or equal to 3%.

Figure 13(b) shows the numerical load–deflection curves for beam U2 obtained using the three stress–strain tension–softening stress–strain laws (i.e. bi–linear, exponential and linear) and all the same modelling options as for Figure 13(a). The results are extremely close to those in Figure 13(a), with differences in all key values below 3%, showing that the choice of using a stress–strain or a stress–displacement law has negligible influence on the load–displacement curve.

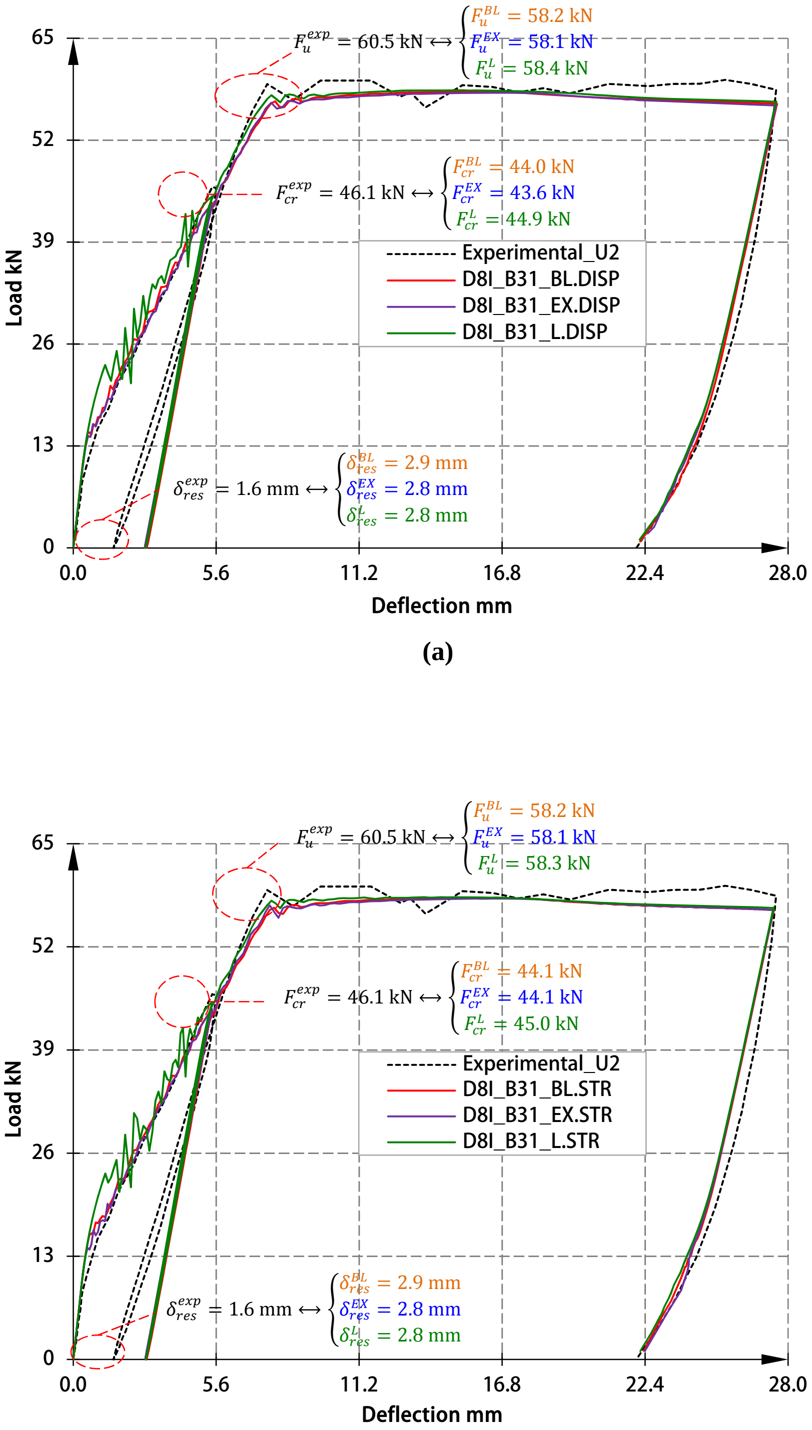

(a)

(b)

Figure 13. Comparison between the experimental and numerical load–deflection curves for beam U2 obtained using: (a) stress–displacement and (b) stress–strain tension–softening laws

Figures 13(a) and 13(b) show that the initial stiffness of the numerical load–deflection curve, predicted using a linear tension–softening law, is higher than that of the experimental response. On the contrary, the initial stiffness of the experimental load–deflection curve is closely predicted using the bi–linear and exponential tension–softening laws.

There is a good agreement between the numerical and experimental curves in the reloading phase (i.e. the rebar post–yielding phase) regardless of the tension–softening law employed in the FE analysis.

It can also be seen from Figures 13(a) and 13(b) that all simulations over–predict the residual deflection upon the first unloading. The numerical results suggest that almost no degradation of the elastic stiffness took place (i.e. the numerical unloading path appears to be undamaged). In turn, this may indicate that the plastic displacements and their associated strains used to define the tensile damage evolution were over–estimated. Despite the difference in the unloading phase, the numerical results obtained for beam U2 demonstrate that the three tension–softening laws investigated in this study can effectively capture the load–deflection response of the four–point bending test. Furthermore, the stress–strain and stress–displacement laws provide practically the same response.

The same simulations were conducted for beam U5, which is 89% and 83% shorter and less deep than beam U2, using identical material parameters and modelling options. For these simulations, Figure 14(a) shows the experimental load–deflection curve for beam U5 compared against the numerical curves obtained using the three stress–displacement tension–softening laws shown in Figure 9(a). Again, C3D8I and B31 elements were used to model concrete, steel rebars and stirrups, respectively. The cracking loads reported in Figure 14(a) are generally over–predicted in the numerical model compared with the corresponding experimental value with differences of 14%, 14% and 19% for the bi–linear, exponential and linear stress–displacement tension–softening laws, respectively. The predicted residual deflections upon the first unloading are also higher than the experimental value, with differences between 21% and 23% for the same tension–softening laws. The experimental ultimate–load is closely predicted by the model with differences of only 5%, 2% and 4% for the bi–linear, exponential and linear tension–softening laws, respectively.

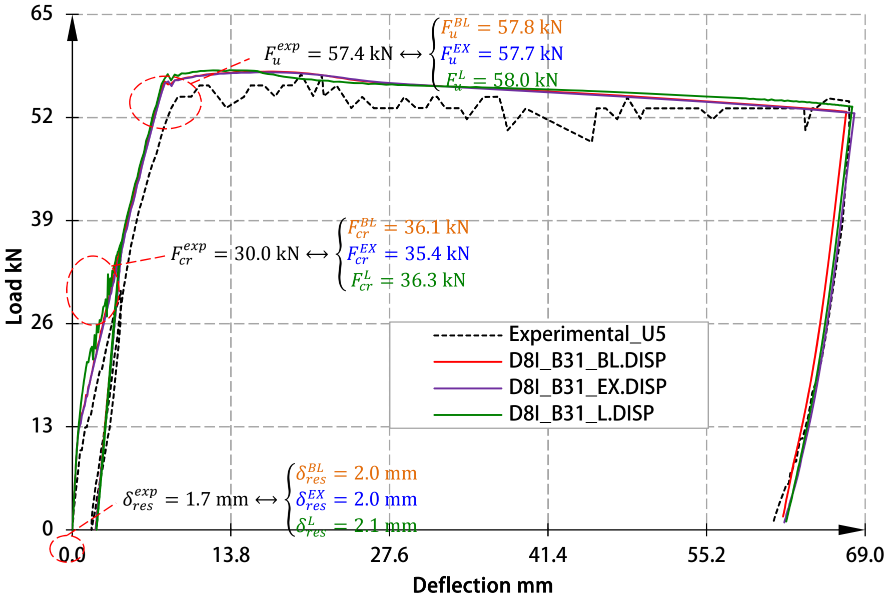

(a)

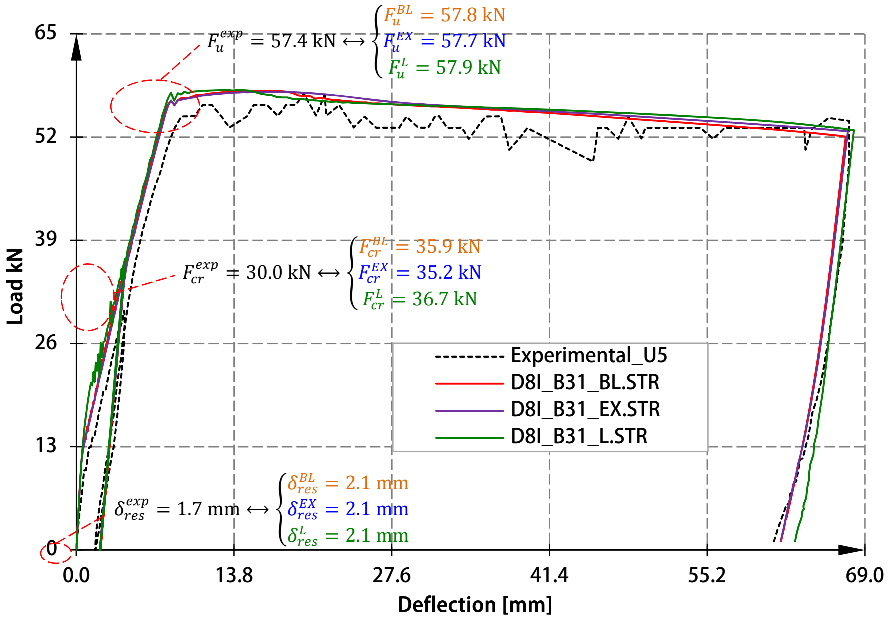

(b)

Figure 14. Comparison between the experimental and numerical load–deflection curves for beam U5 obtained using: (a) stress–displacement tension–softening; (b) stress–strain tension–softening laws

Figure 14(b) shows the equivalent numerical–experimental comparison using stress–strain tension–softening laws instead of stress–displacement laws, and these again employ linear, exponential and bi–linear approaches. The predicted cracking loads, residual deflections and ultimate–loads are reported in Figure 14(b). The cracking loads are over–predicted by the model relative to the corresponding experimental values by around 15% to 18%. The predicted residual deflections upon the first unloading are also higher than the experimental value, with differences between 20% and 23%. The ultimate–load is closely predicted by the model with differences of only 2%, 2% and 5% for the bi–linear, exponential and linear tension–softening laws, respectively.

It can be seen from Figure 14(a) that the bi–linear and exponential tension–softening laws predict an identical initial stiffness, despite being slightly over–estimated, whereas the linear law predicts a higher initial stiffness, as for beam U2. Furthermore, the three tension–softening laws behave almost similarly in the post–yielding phase of the steel rebars. A similar observation can also be seen in Figure 14(b), with the exception that the exponential stress–strain tension–softening law (i.e. D8I_B31_EX.STR) tends to be closer to the experimental curve in the advanced post–yield response. There is generally a reasonably good agreement between the experimental load–deflection curve and its numerical counterpart regardless of the tension–softening law used in the FE model. This further confirms the effectiveness of the three tension–softening laws investigated in this study and more generally the modelling approach.

The conclusions that can be drawn from the results are twofold. Firstly, the assumption of a stress–strain or a stress–displacement approach has a small impact on the predicted numerical solution providing that an adequate mesh aspect ratio is selected. Generally, a mesh size, which has an aspect ratio (i.e. the ratio between the longest length to the shortest length of a finite–element) as close as possible to unity, is most ideal. In addition, if some elements in the FE mesh have large aspect ratios, it is likely that they will exhibit different cracking behaviour depending on the direction of cracking. The second main conclusion is that the shape of the tension–softening law, that is linear, bi–linear or exponential, has a relatively small influence on the behaviour. The linear law provides a stiffer response in the post–cracking part before yielding.

4-1-3. Effects of Element Types Used for Steel Rebars

As concluded in the previous section, all tension–softening laws predict very similar results compared with the experimental response for beams U2 and U5. Therefore, due to space limitations, the numerical results predicted using the exponential law are presented and discussed herein.

In Figure 15, the experimental load–deflection curve for beam U2 is compared against four numerical curves obtained using a structured mesh of C3D8I elements to model the concrete. The first two numerical curves, coded B31_GL and B31_GNL, was obtained using beam elements (B31) to model the steel rebars and geometric linear (GL) and nonlinear (GNL) models, respectively. Likewise, the other two numerical curves, coded T3D2_GL and T3D2_GNL, were obtained using truss elements (T3D2) for the rebars, again with GL and GNL model, respectively. Figure 16 shows the same results for beam U5.

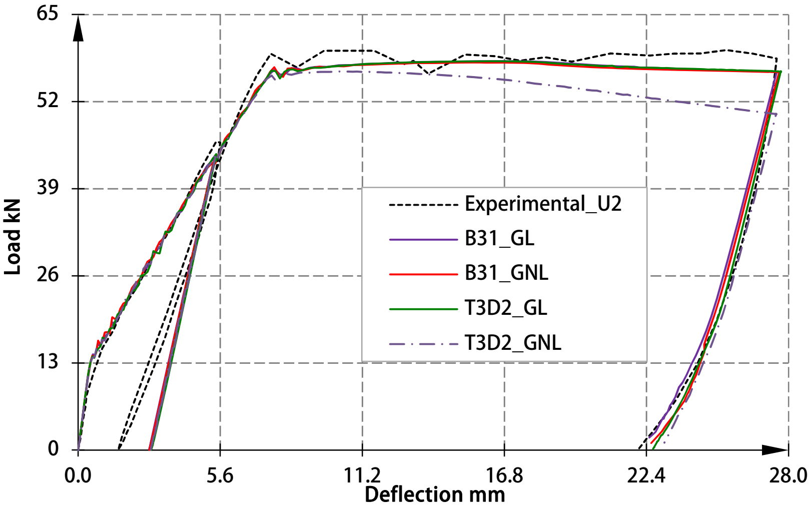

Figure 15. Numerical load–deflection curves predicted for beam U2 using truss and beam elements to model steel rebars, compared against the experimental curve

Figures 15 and 16 show that all curves predicted the same response up to the cracking load. These curves also predicted identical residual deflections. The numerical curves in Figure 15 present small differences in the reloading phase, particularly, after the yield point. Using beam or truss elements leads to practically no difference if a GL model is used, whereas with truss elements and a GNL model an early softening response is found, consistently for both beams U2 and U5. The only difference in Figure 16 is that beam elements and a GNL model lead to a curve that starts to soften beyond a prescribed displacement of about 40 mm. It is also noteworthy that beam U5 was loaded in the experiment up to a larger level of ductility with respect to U2.

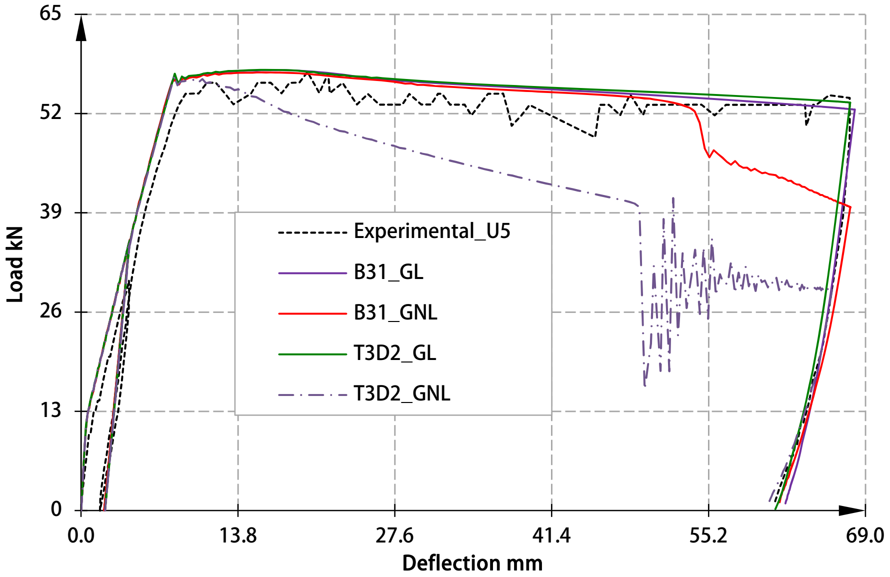

Figure 16. Numerical load–deflection curves predicted for beam U5 using truss and beam elements to model steel rebars, compared against the experimental curve

Figures 15 and 16 show that the geometric nonlinearity appears to have a significant impact on the structural response when truss elements are used. In a large displacement–analysis, ABAQUS treats truss elements as an incompressible material regardless of the actual material definition (Dassault Systèmes 2014a). It appears that the prescribed displacement applied in the FE conducted simulations may have caused a significant longitudinal stretch to the steel rebars being modelled as truss elements in this case. This was confirmed by the observation of high values for the maximum principal nominal and logarithmic strains numerically predicted along the rebar axes. Here, it can be argued that these high magnitudes of longitudinal strains caused not only a significant stretching in the rebars but also a significant reduction of their cross–sectional area.

It is known that in a large–displacement analysis, the current configuration is used to formulate the element, rather than the reference configuration. Hence, the higher the deformation the element is subjected to, the greater the distortion that will occur. This suggests that the inclusion of large–displacement effects in the FE model is ultimately of great influence on the structural behaviour being analysed, and that truss elements may not be the ideal choice to model steel rebars if geometric nonlinearity is considered in the simulation.

4-1-4. Effects of Mesh and Element Types Used for Concrete

In this section, the numerical load–defection curves obtained using two mesh types to model the concrete, structured meshes of 3D linear (8–noded) elements with incompatible strains (C3D8I) and 3D linear elements with reduced integration (C3D8R), and unstructured meshes of 3D linear (4–noded) or 3D quadratic (10–noded) tetrahedral (C3D4 and C3D10M, respectively) elements, are presented. As before, the exponential stress–strain tension–softening law was employed. The steel rebars were modelled using linear beam (B31) elements with the structured meshes of C3D8I and C3D8R elements as well as with the unstructured mesh of C3D4 element, and quadratic beam (B32) elements with the unstructured mesh of C3D10M elements.

The four numerical curves in Figure 17 are almost identical, with all three numerical curves predicted using C3D8R, C3D4 and C3D10M elements predicting a slightly stiffer response relative to the experimental one. With all elements, there is generally a good agreement between the numerical and the experimental curves.

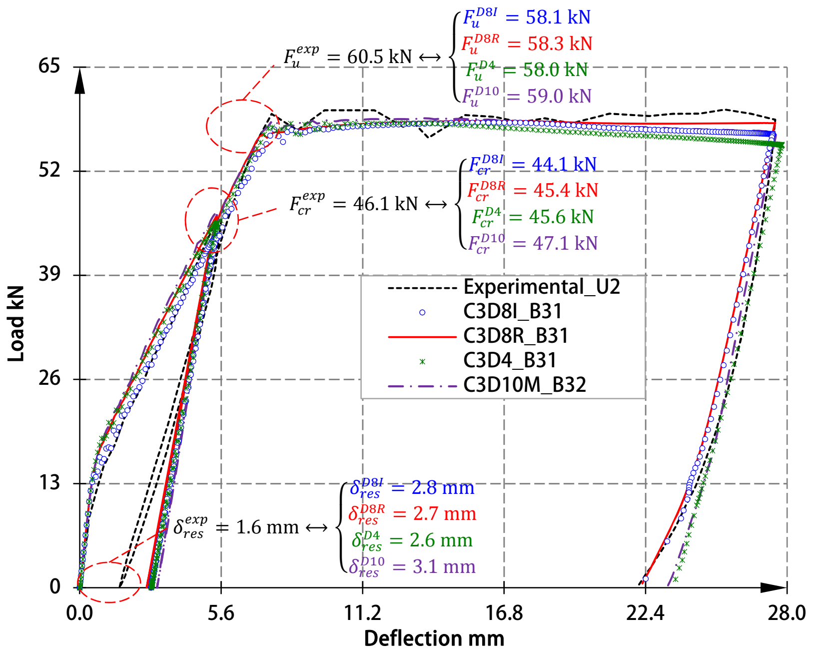

Figure 17. Numerical load–deflection curves for beam U2 obtained using four different mesh types to model the concrete

Figure 18 compares the experimental load–deflection curve for beam U5 against the numerical curves obtained using the four meshes and element types mentioned earlier in this section. The numerical observations noted during discussions on the results for beam U2 can be extended to beam U5. The differences between the curves are very small except that C3D10M elements lead to a slightly stiffer response. The results predicted with C3D8I and C3D4 elements show some limited amount of softening.

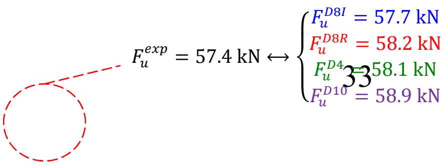

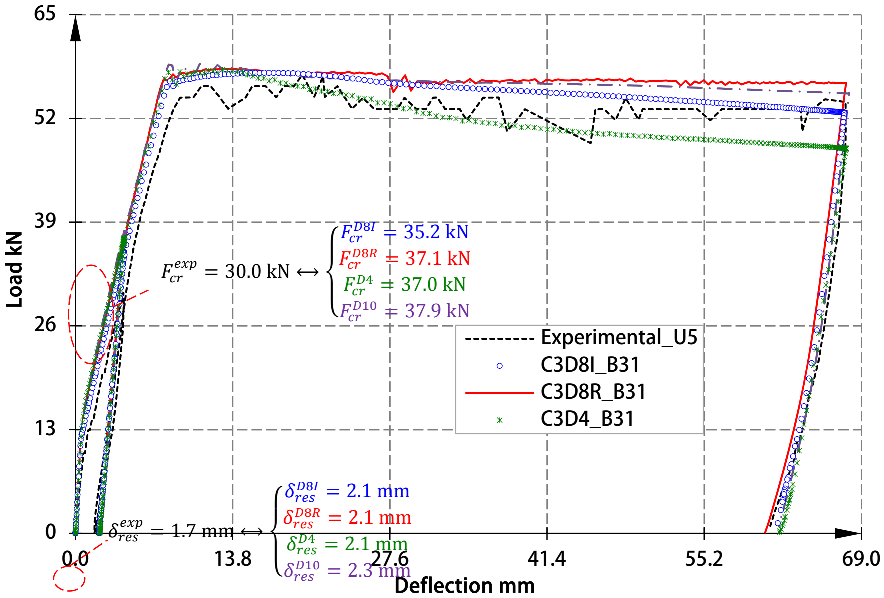

Figure 18. Numerical load–deflection curves for beam U5 obtained using different element and mesh types to model

The slightly increased stiffness when using an unstructured mesh of C3D4 and C3D10M elements can be attributed to the estimation of the element characteristic length (ECL) being used to convert a stress–displacement tension–softening law into a stress–strain law, as discussed before in defining the Tensile . Given the irregular shape of both linear and quadratic tetrahedral elements, the crack length is chosen to be representative of all the finite–elements in any prospective mesh, and is taken as the mean value of the average maximum and minimum element edge lengths. For example, in one of the unstructured meshes presented in this work, in which a 10 mm approximate finite–element size was used, the average maximum edge length was 15.70 mm and the average minimum edge length was 10.26 mm. Hence, the ECL for an unstructured mesh of C3D4 elements was estimated as the average of these two values as 12.98 mm, and for an unstructured mesh of C3D10M elements, the ECL was estimated as 0.5 × 12.98 mm. Although it can be argued that these characteristic lengths are slightly under–estimated (i.e. a higher ECL would have resulted in lower cracking strains and therefore, a reduced stiffness of the numerical curve), it is also possible that the crack–opening displacements, from which the cracking strains were obtained as per the crack band model, are slightly over–estimated.

4-1-5. Effects of Mesh Size

Figures 19 and 20 present comparisons between the experimental curves for beams U2 and U5, respectively, and three numerical curves obtained using three different densities of unstructured meshes of C3D10M elements and structured meshes of C3D8I elements for beams U2 and U5, respectively. Mesh densities are indicated herein as the ratio between the average length of the FE edge and the height, h, of the RC beam studied. Similar results for each beam were obtained for all types of elements, so only the aforementioned types of elements for the two beams are presented here. Three mesh densities of about 0.04, 0.06 and 0.08 are chosen, so that the aspect ratio of the resulting FE mesh has a value close to unity. It is observed that the three mesh densities predict almost the same load–deflection response. Similar results were found for mesh–convergence analyses for structured meshes used for beam U2 and unstructured meshes used for beam U5.

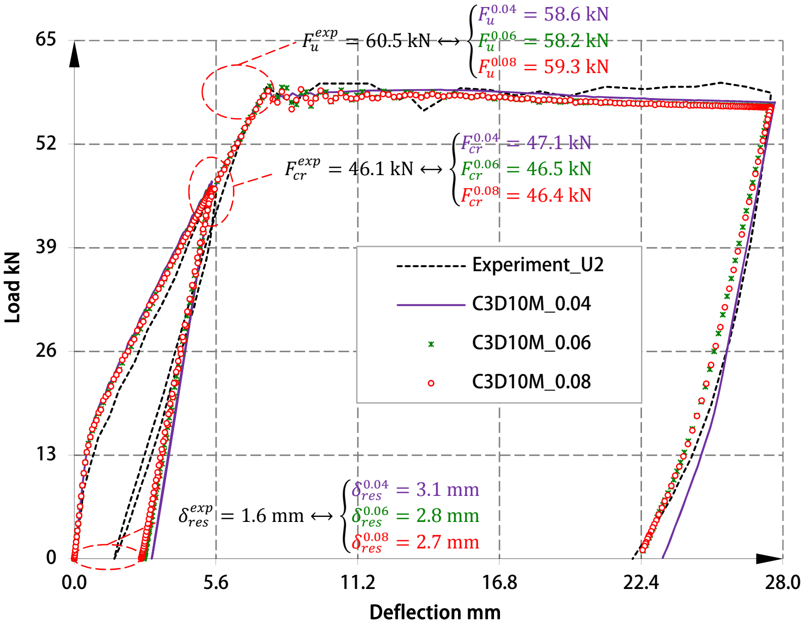

Figure 19. Numerical load–deflection curves for beam U2 obtained using three different sizes of unstructured meshes of C3D10M elements

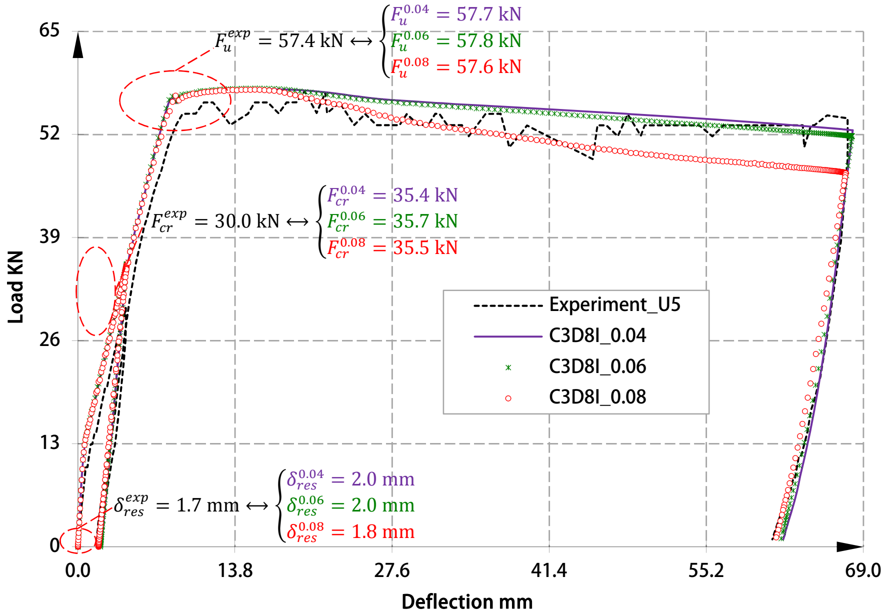

Figure 20. Numerical load–deflection curves for beam U5 obtained using three different sizes of structured meshes of C3D8I elements

It is concluded that the coarser of the meshes used is sufficiently refined if the load–deflection curve is the main result of interest. Some differences were found between the predicted crack patterns as discussed below.

4-2. Crack Patterns

Cracks at the material integration points cannot be explicitly output when using the CDP model employed in this study. Nevertheless, the crack patterns can be graphically represented by introducing an effective crack direction. For the latter, Lubliner et al. (1989) assumes that cracks are initiated at points where the tensile equivalent plastic strain, $\tilde{\varepsilon}_t^{pl}$, and the maximum principal plastic strain are both positive. The direction of the latter strain, as it is normal to the crack plane, determines the crack direction. Following the preceding criterion to determine the predicted crack patterns, the contour plots of the maximum principal inelastic strain are reported in this section.

Figures 21(a) and 21(b) show the contour plots of the maximum principal inelastic strain for beam U2 at the ultimate–load using a structured mesh of C3D8I and C3D8R elements with corresponding prescribed displacements of 15.8 mm and 14.4 mm, respectively. In Figure 21(a), the nine cracks, labelled as crack no. 5 to crack no. 13, propagate initially vertically and rightwards towards the displacement–application point. On the other hand, the tensile cracks initially propagate vertically and leftwards towards the region where displacement is applied. The tensile cracks formed in the constant–moment region (i.e. crack no. 1 to crack no. 4) initially propagate vertically and slightly leftwards again towards to displacement–application point. Tensile cracks can also be observed at the bottom of beam U2, mainly, along the steel reinforcement level (e.g. cracks no. 8, 9 and 10), indicating slipping between concrete and steel rebars. Comparing Figures 21(a) and 21(b), one can observe that there are some discrepancies between the crack patterns predicted using structured meshes of C3D8I or C3D8R elements. A little fewer cracks form in the latter (i.e. eight instead of nine cracks formed in the shear–span region, and three instead of four main cracks formed in the constant–moment region). Furthermore, the cracks predicted using a structured mesh of C3D8R elements, particularly those formed in the constant–moment region, appear to be significantly wider than those predicted using a structured mesh of C3D8I elements.

Figures 21(c) and 21(d) show the predicted crack patterns for beam U2 at the ultimate–load using an unstructured mesh of C3D4 and C3D10M elements with corresponding prescribed displacements of 12.8 mm and 13.6 mm, respectively. The key difference between cracks predicted using these two unstructured meshes and those formed in the structured meshes is that in the unstructured mesh, there is no mesh bias, particularly in the shear–span region where cracks are expected to be inclined as a result of shear. It can also be observed that although a similar number of cracks formed in the shear–span region in Figures 21(c) and 21(d) (i.e. 9 cracks in total), their initiation and propagation are quite different. For instance, while crack no. 5 in both figures appear to be initiated at the same position, the initiation of crack no. 6 occurred in a different position. Again, cracks can also be seen at the interface between the bottom rebars and concrete.

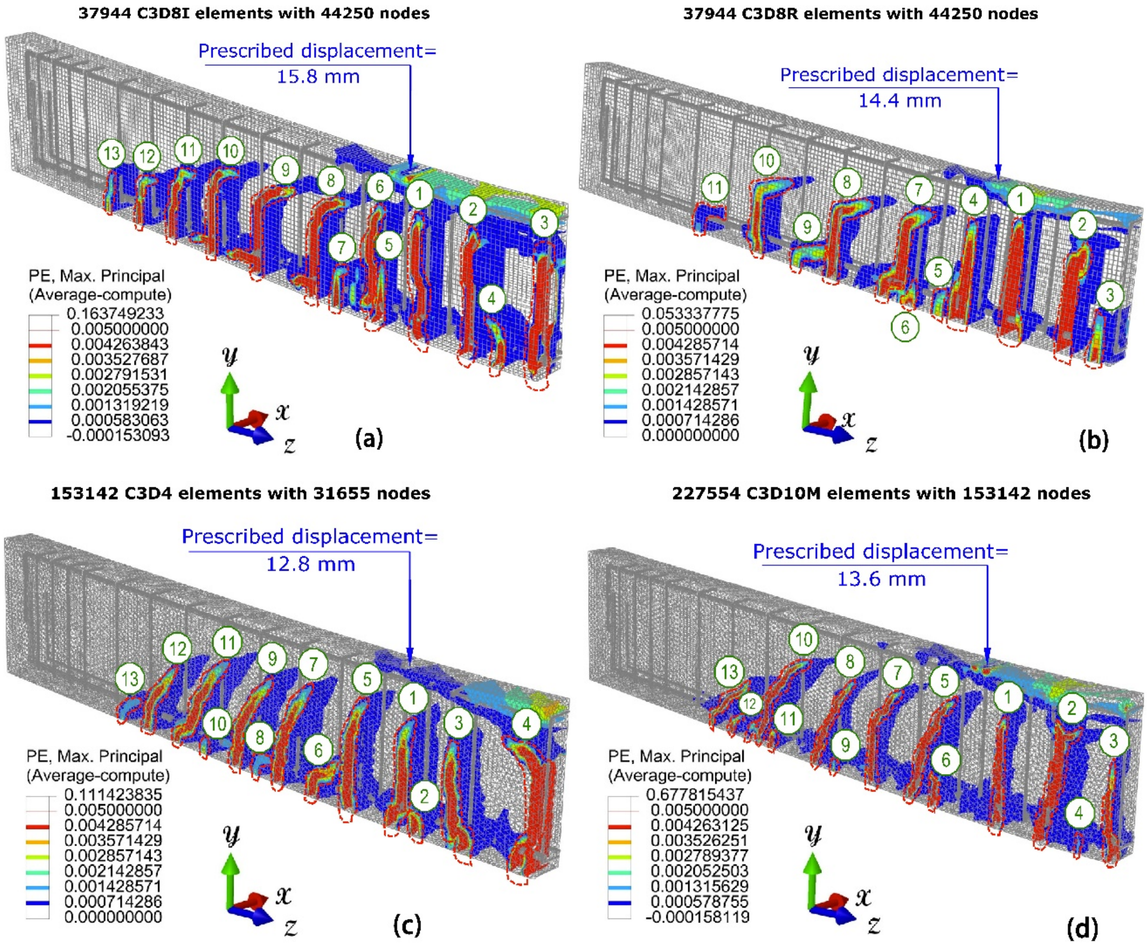

Figure 21. Predicted crack patterns for beam U2 at the ultimate–load using structured meshes of (a) C3D8I and (b) C3D8R elements, and unstructured meshes of (c) C3D4 and (d) C3D10M elements

Figures 22(a) to 22(c) show the predicted crack patterns for beam U2 at the ultimate–load using unstructured meshes of three different mesh densities of C3D10M elements with corresponding prescribed displacement of 12.1 mm, 7.2 mm and 7.2 mm, respectively. For the finest mesh (i.e. Figure 22(a)), a larger number of cracks formed and propagated along the beam span compared to the other two coarser meshes.

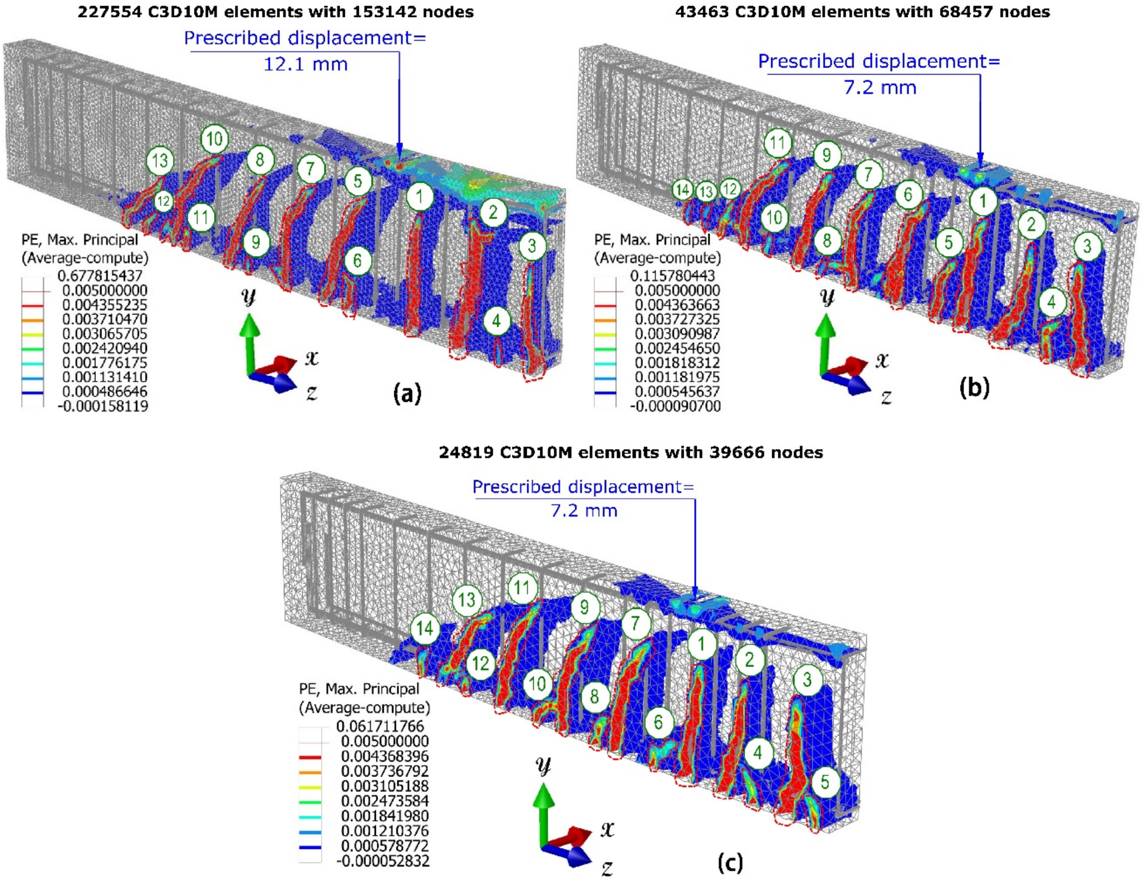

Figure 22. Predicted crack patterns for beam U2 at the ultimate–load using unstructured meshes of C3D10M elements with sizes of (a) 0.04, (b) 0.06 and (c) 0.08

Figure 23(a) to 23(d) show the corresponding results for beam U5 at the ultimate–load, at prescribed displacements of 13.8 mm and 10.3 mm, respectively, for structured meshes of C3D8I and C3D8R elements, and prescribed displacements of 10.8 mm and 7.3 mm, respectively, for unstructured meshes of C3D4 and C3D10M elements. Similar to the observation noted on the predicted crack patterns for beam U2, the structured meshes used for beam U5 showed some mesh bias, whereas this bias was less pronounced for the unstructured mesh case. It can be also seen from comparing the predicted crack patterns for beam U5 with those experimentally observed, shown in Figure 24, that the unstructured meshes captured relatively well most of the cracks in the constant–moment region.

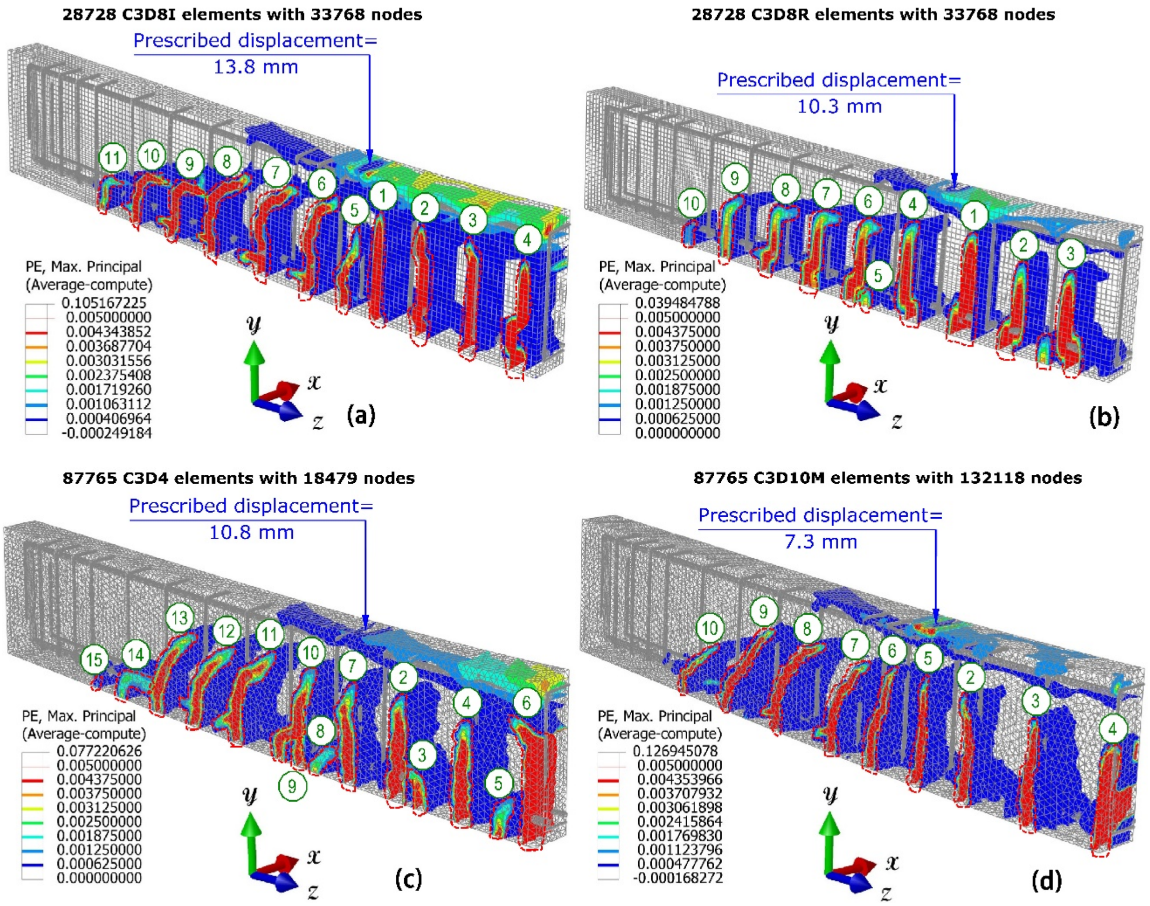

Figure 23. Predicted crack patterns for beam U5 at the ultimate–load using structured meshes of (a) C3D8I and (b) C3D8R elements, and unstrauctured meshes of (c) C3D4 and (d) C3D10M elements

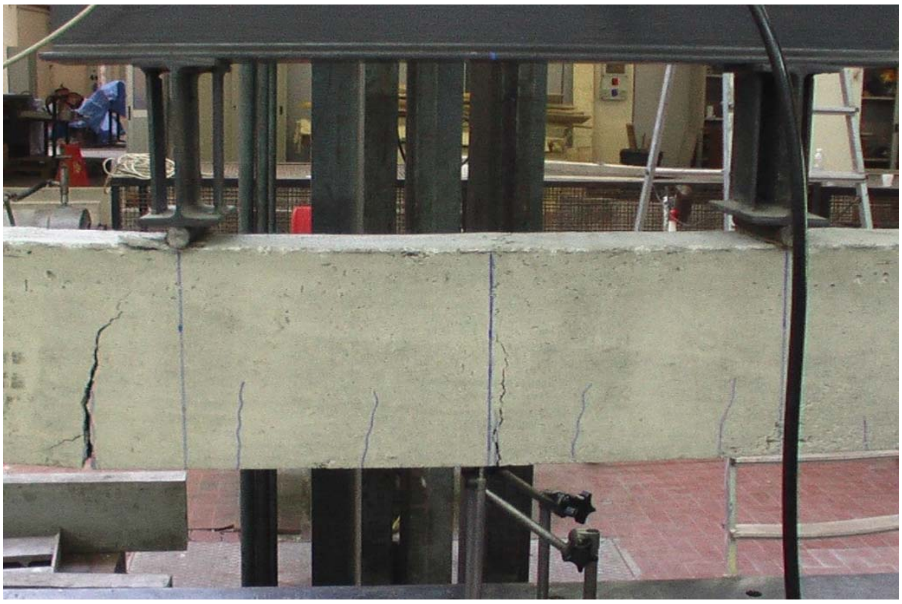

Figure 24. Crack patterns experimentally observed for beam U5 (Alfano, De Cicco et al. 2012)

Figure 25(a) to 25(d) show the predicted crack patterns for beam U5 at the ultimate–load using structured meshes of four different sizes of C3D8I elements with corresponding prescribed displacements of 14.6 mm, 14.5 mm, 12.2 mm and 12.7 mm, respectively. It is worth noting here that the element sizes in this case were chosen so that the resulting aspect ratio had a unity value. The crack numbers indicate the sequence of the crack formation. It can be seen that the finer the mesh, the clearer the predicted cracks. The strain contours of the coarse mesh in Figure 25(d) does not represent with repeatable accuracy the crack patterns. Furthermore, the predicted cracks tend to localise along one column or two of finite–elements. Therefore, wider cracks are predicted in a coarse mesh as opposed to narrower ones in a fine mesh (e.g. cracks no. 3 and 4 in Figure 25(d) and cracks no. 1 and 2 in Figure 25(a)).

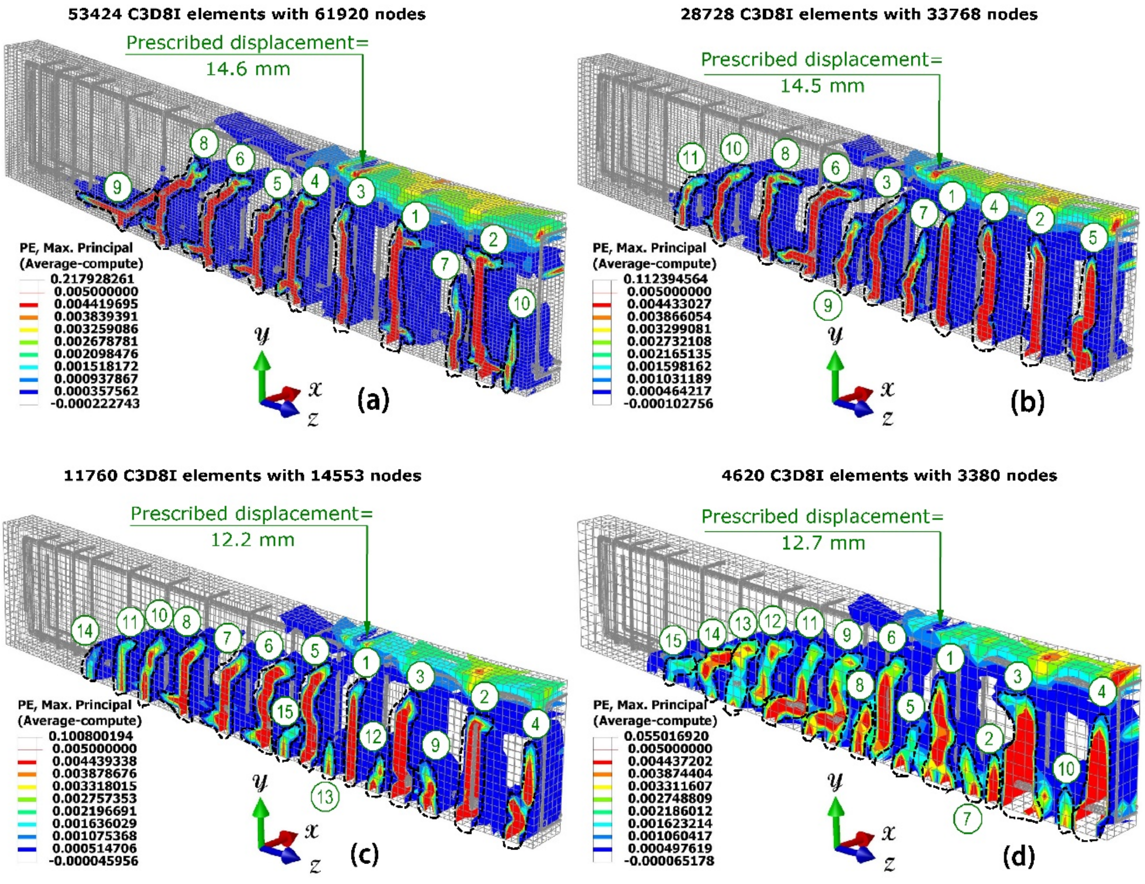

Figure 25. Predicted crack patterns for beam U5 at the ultimate–load using structured meshes of C3D8I elements with sizes of: (a) 0.03 mm^3, (b) 0.04 and (c) 0.06 and (d) 0.08 mm^3

5. Conclusions

In this paper, three–dimensional nonlinear finite–element models have been developed to study the flexural behaviour of two reinforced–concrete beams under four–point bending. A dynamic explicit procedure together with the concrete damaged–plasticity model are employed to simulate the loading–unloading–reloading behaviour of the beams and to predict their crack patterns. The validation and the comparative analyses of the different model choices considered are particularly meaningful for two reasons. Firstly, identical material properties are used in the finite–element models for both beams. Secondly, many material parameters are determined directly based on the measured material properties as reported by Alfano et al. (2012) while the remaining few parameters requiring some calibration were found to be well within the expected range of values. Moreover, the sensitivity of the results to these terms has been explicitly examined in this paper.

The effect of the tension–softening law on the load–deflection response has been studied. The laws considered are a post–failure stress–displacement or stress–stain relationship, with each having either a bi–linear, exponential or linear response. For all the laws included in this study, the predicted load–deflection curves are in very good agreement with the corresponding experimental values. The curves predicted using the linear law over–estimated the initial stiffness very slightly but provided excellent agreement with the experimental response in the post–yielding phase.

The effect of modelling steel rebars on the overall response of the two reinforced–concrete beams has been also investigated. To this end, beam and truss elements are considered. No differences were found for a geometrically linear analysis; therefore, the dowel action was not representative. By contrast, for a geometrically nonlinear analysis, the load–deflection curves predicted using truss elements exhibited significant softening beyond the ultimate–load, whilst those predicted using beam elements exhibited no or negligible softening and good agreement with experiments were found. This may be important to consider when studying the progressive collapse of reinforced–concrete structures.

The effect on the load–deflection response of the selection of the element and mesh types used to model the concrete has also been presented. Structured meshes of linear (8–noded) elements with incompatible strains or with reduced integration, and unstructured meshes of linear (4–noded) and quadratic (10–noded) tetrahedral elements, are considered. The disparities between the results when different element types were used was found to be very small. Mesh–convergence analyses were also presented to confirm that the meshes used in these analyses were sufficiently refined and that further mesh refinement would provide negligible influence on the load–deflection curves. However, the crack patterns predicted using different mesh sizes presented some discrepancies, in that, for finer meshes more cracks were found to develop.

Finally, the predicted crack patterns using structured and unstructured meshes have been presented and discussed. As expected, structured meshes exhibited some mesh bias in terms of the predicted maximum principal inelastic strain, whereas this bias was less pronounced in cases involving unstructured meshes.

Acknowledgements

The first author wishes to gratefully acknowledge the financial support provided by Damascus University and the British Council for his study at Brunel University London.

References

AHMED, A., 2014. Modeling of a Reinforced Concrete Beam Subjected to Impact Vibration using ABAQUS. *International Journal of Civil & Structural Engineering,* **4**(3), pp. 227-236.

ALFANO, G., DE CICCO, F. and PROTA, A., 2012. Intermediate Debonding Failure of RC Beams Retrofitted in Flexure with FRP: Experimental Results versus Prediction of Codes of Practice. *Journal of Composites for Construction,* **16**(2), pp. 185-195.

ARSLAN, G., 2007. Sensitivity Study of the Drucker–Prager Modeling Parameters in the Prediction of the Nonlinear Response of Reinforced Concrete Structures. *Materials & Design,* **28**(10), pp. 2596-2603.

BAŽANT, Z.P., 1986. Mechanics of Distributed Cracking. *Applied Mechanics Reviews,* **39**(5), pp. 675-705.

BAŽANT, Z.P., 1980. Fracture Mechanics of Reinforced Concrete. *Journal of the Engineering Mechanics Division,* **106**(6), pp. 1287-1306.

BAŽANT, Z.P., 1976. Instability, Ductility and Size Effect in Strain-Softening Concrete. *Journal of the Engineering Mechanics Division,* **102**(2), pp. 331-344.

BAŽANT, Z.P. and BECQ-GIRAUDON, E., 2002. Statistical Prediction of Fracture Parameters of Concrete and Implications for Choice of Testing Standard. *Cement and Concrete Research,* **32**(4), pp. 529-556.

BAŽANT, Z.P. and PLANAS, J., 1998. *Fracture and Size Effect in Concrete and other Quasibrittle Materials.* Boca Raton: CRC Press.

BELYTSCHKO, T., MOËS, N., USUI, S. and PARIMI, C., 2001. Arbitrary Discontinuities in Finite Elements. *International Journal for Numerical Methods in Engineering,* **50**(4), pp. 993-1013.

BRESLER, B. and PISTER, K.S., 1958. Strength of Concrete Under Combined Stresses. *ACI Journal Proceedings,* **55**(9), pp. 321-345.

BRITISH STANDARD INSTITUTION, 2004. *Eurocode 2: Design of Concrete Structures: Part 1-1: General Rules and Rules for Buildings.* London: CEN.

BRITISH STANDARD INSTITUTION, 2000. *Concrete - Part 1: Specification, performance, production and conformity.* London: CEN.

BUYUKOZTURK, O., 1977. Nonlinear Analysis of Reinforced Concrete Structures. *Computers & Structures,* **7**(1), pp. 149-156.

CEB-FIP, M., 1993. *Design of Concrete Structures. CEB-FIP-Model-Code 1990.* London: British Standard Institution.

CERVANTES, I., 2013. *Flexural Retrofitting of Reinforced Concrete Structures using Green Natural Fiber Reinforced Polymer Plates*, California State University, Department of Civil Engineering and Construction Engineering Management, Long Beach.

CHEN, G.M., CHEN, J.F. and TENG, J.G., 2012. On the Finite Element Modelling of RC Beams Shear–Strengthened with FRP. *Construction and Building Materials*, **32**, pp. 13-26.

CHEN, G.M., TENG, J.G. and CHEN, J.F., 2011. Finite–Element Modeling of Intermediate Crack Debonding in FRP–Plated RC Beams. *Journal of Composites for Construction,* **15**(3), pp. 339-353.

COPE, R.J., RAO, P.V., CLARK, L.A. and NORRIS, R., 1980. Modeling of Reinforced Concrete Behavior for Finite Element Analysis of Bridge Slabs. In: R.L. TAYLOR, E. HINTON and D.R.J. ODEN, eds, *Numerical Methods for Nonlinear Problems 1.* Pineridge Press, Swansea, pp. 457-470.

CORNELISSEN, H.A.W., HORDIJK, D.A. and REINHARDT, H.W., 1986. Experimental Determination of Crack Softening Characteristics of Normalweight and Lightweight Concrete. *Heron,* **31**(2), pp. 45-56.

CORONADO, C.A. and LOPEZ, M.M., 2006. Sensitivity Analysis of Reinforced Concrete Beams Strengthened with FRP Laminates. *Cement and Concrete Composites,* **28**(1), pp. 102-114.

DASSAULT SYSTÈMES, 2014a. *ABAQUS 6.14 Analysis User's Guide, Volume III: Materials.* USA.

DASSAULT SYSTÈMES, 2014b. *ABAQUS 6.14 Analysis User's Guide, Volume V: Prescribed Conditions, Constraints and Interactions.* USA: Dassault Systèmes.

DASSAULT SYSTÈMES, 2014c. *ABAQUS Example Problems Guide, Volume I: Static and Dynamic Analyses.* USA.

DRUCKER, D.C. and PRAGER, W., 1952. Soil Mechanics and Plastic Analysis for Limit Design. *Quarterly of Applied Mathematics,* **10**(2), pp. 157-165.

DVORKIN, E.N., CUITIÑO, A.M. and GIOIA, G., 1990. Finite Elements with Displacement Interpolated Embedded Localization Lines Insensitive to Mesh Size and Distortions. *International Journal for Numerical Methods in Engineering,* **30**(3), pp. 541-564.

FOSTER, S.J., BUDIONO, B. and GILBERT, R.I., 1996. Rotating Crack Finite Element Model for Reinforced Concrete Structures. *Computers & Structures,* **58**(1), pp. 43-50.

GENTILI, F. and PETRINI, F., 2016. On the Role of the Numerical Analyses in Forensic Investigations of Fire-Induced Progressive Collapses of Tall Buildings. *International Journal of Forensic Engineering,* **3**(1-2), pp. 45-68.

GŁODKOWSKA, W. and RUCHWA, M., 2010. Static Analysis of Reinforced Concrete Beams Strengthened with CFRP Composites. *Archives of Civil Engineering,* **56**(2), pp. 111-122.

GUPTA, A.K. and AKBAR, H., 1984. Cracking in Reinforced Concrete Analysis. *Journal of Structural Engineering,* **110**(8), pp. 1735-1746.

HILLERBORG, A., 1985. The Theoretical Basis of a Method to Determine the Fracture Energy Gf of Concrete. *Materials and Structures,* **18**(4), pp. 291-296.

HILLERBORG, A., MODÉER, M. and PETERSSON, P.E., 1976. Analysis of Crack Formation and Crack Growth in Concrete by means of Fracture Mechanics and Finite Elements. *Cement and Concrete Research,* **6**(6), pp. 773-781.

HORDIJK, D.A., 1991. *Local Approach to Fatigue of Concrete*, Delft University of Technology.

HSIEH, S.S., CHEN, W.F. and TING, E.C., 1979. An Elastic—Fracture Model for Concrete, *Engineering Mechanics* 1979, ASCE, pp. 437-440.

HUEBNER, K.H., DEWHIRST, D.L., SMITH, D.E. and BYROM, T.G., 2008. *The Finite Element Method for Engineers.* 4th Edition edn. John Wiley & Sons.

JANKOWIAK, I., 2012. Analysis of RC Beams Strengthened by CFRP Strips–Experimental and FEA Study. *Archives of Civil and Mechanical Engineering,* **12**(3), pp. 376-388.

JIANG, H., WANG, X. and HE, S., 2012. Numerical Simulation of Impact Tests on Reinforced Concrete Beams. *Materials & Design,* **39**, pp. 111-120.

JIRÁSEK, M. and ZIMMERMANN, T., 1998. Analysis of Rotating Crack Model. *Journal of Engineering Mechanics,* **124**(8), pp. 842-851.

LEE, J. and FENVES, G.L., 1998. Plastic–Damage Model for Cyclic Loading of Concrete Structures. *Journal of Engineering Mechanics,* **124**(8), pp. 892-900.

LOTFI, H.R. and SHING, P.B., 1995. Embedded Representation of Fracture in Concrete with Mixed Finite Elements. *International Journal for Numerical Methods in Engineering,* **38**(8), pp. 1307-1325.

LUBLINER, J., OLIVER, J., OLLER, S. and ONATE, E., 1989. A Plastic–Damage Model for Concrete. *International Journal of Solids and Structures,* **25**(3), pp. 299-326.

MANZOLI, O.L., GAMINO, A.L., RODRIGUES, E. and CLARO, G., 2012. Modeling of Interfaces in Two-Dimensional Problems using Solid Finite Elements with High Aspect Ratio. *Computers & Structures,* **94**, pp. 70-82.

MARKOU, G. and PAPADRAKAKIS, M., 2012. Modeling of Reinforced Concrete Structures with 3D Detailed Finite Element Models. *A Bi-Annual, Refereed Journal Published by ALHOSN University, Abu Dhabi, UAE,* **4**(2), pp. 47-63.

MILFORD, R.V. and SCHNOBRICH, W.C., 1985. The Application of the Rotating Crack Model to the Analysis of Reinforced Concrete Shells. *Computers & Structures,* **20**(1), pp. 225-234.

NGO, D. and SCORDELIS, A.C., 1967. Finite Element Analysis of Reinforced Concrete Beams. *American Concrete Institute,* **64**(3), pp. 152-163.

NILFOROUSH HAMEDANI, R. and SHAHROKH ESFAHANI, M., 2012. *Numerical Evaluation of Structural Behavior of the Simply Supported FRP–RC Beams*, Royal Institute of Technology (KTM), Division of Structural Engineering and Bridges, Stockholm, Sweden.

NILSON, A.H., 1968. Nonlinear Analysis of Reinforced Concrete by the Finite Element Method. *ACI Journal Proceedings,* **65**(9), pp. 757-766.

OBAIDAT, Y.T., DAHLBLOM, O. and HEYDEN, S., 2010. Nonlinear FE Modelling of Shear Behaviour in RC Beam Retrofitted with CFRP, BIĆANIĆ ET AL., ed. In: *Computational Modelling of Concrete Structures* 2010, Taylor & Francis Group, pp. 49-56.

OBAIDAT, Y.T., HEYDEN, S. and DAHLBLOM, O., 2010. The effect of CFRP and CFRP/Concrete Interface Models when Modelling Retrofitted RC Beams with FEM. *Composite Structures,* **92**(6), pp. 1391-1398.

OLIVEIRA, D.A., 2009. *Back-Analysis Based on the Pinheiros Station Collapse.* Australia: Australasian Tunnelling Society (ATS).

OLIVER, J., 1996. Modelling Strong Discontinuities in Solid Mechanics via Strain Softening Constitutive Equations. Part 2: Numerical Simulation. *International Journal for Numerical Methods in Engineering,* **39**(21), pp. 3601-3623.

OLIVER, J., LINERO, D.L., HUESPE, A.E. and MANZOLI, O.L., 2008. Two–Dimensional Modeling of Material Failure in Reinforced Concrete by means of a Continuum Strong discontinuity Approach. *Computer Methods in Applied Mechanics and Engineering,* **197**(5), pp. 332-348.

OTTOSEN, N.S., 1977. A failure Criterion for Concrete. *Journal of the Engineering Mechanics Division,* **103**(4), pp. 527-535.

OŽBOLT, J., LETTOW, S. and KOŽAR, I., 2002. Discrete Bond Element for 3D Finite Element Analysis of Reinforced Concrete Structures, *Proceedings of the 3rd International Symposium: Bond in Concrete-from research to standards.* 2002, pp. 1-11.

PARK, K., PAULINO, G.H. and ROESLER, J.R., 2008. Determination of the Kink Point in the Bilinear Softening Model for Concrete. *Engineering Fracture Mechanics,* **75**(13), pp. 3806-3818.

PARK, P. and KLINGNER, R.E., 1997. Nonlinear Analysis of RC Members Using Plasticity with Multiple Failure Criteria. *Journal of Structural Engineering,* **123**(5), pp. 643-651.

PLANAS, J., ELICES, M. and GUINEA, G.V., 1992. Measurement of the Fracture Energy using Three-Point Bend Tests: Part 2—Influence of Bulk Energy Dissipation. *Materials and Structures,* **25**(5), pp. 305-312.

RADFAR, S., FORET, G. and SAB, K., 2012. Failure Mode Analysis of Fibre Reinforced Polymer Plated Reinforced Concrete Beams, *6th International Conference on FRP Composites in Civil Engineering*, 13 June 2012, pp. 1-8.

RASHID, Y.R., 1968. Ultimate Strength Analysis of Prestressed Concrete Pressure Vessels. *Nuclear Engineering and Design,* **7**(4), pp. 334-344.

ROESLER, J., PAULINO, G.H., PARK, K. and GAEDICKE, C., 2007. Concrete Fracture Prediction using Bilinear Softening. *Cement and Concrete Composites,* **29**(4), pp. 300-312.

SIMO, J.C. and RIFAI, M., 1990. A Class of Mixed Assumed Strain Methods and the Method of Incompatible Modes. *International Journal for Numerical Methods in Engineering,* **29**(8), pp. 1595-1638.

SINAEI, H., SHARIATI, M., HOSEIN ABNA, A., AGHAEI, M. and SHARIATI, A., 2012. Evaluation of Reinforced Concrete Beam Behaviour using Finite Element Analysis by ABAQUS. *Scientific Research and Essays,* **7**(21), pp. 2002-2009.

SOLOMOS, G., CASADEI, F., GIANNOPOULOS, G. and LARCHER, M., 2011. Experimental and Numerical Simulation Activities for the Assessment of Explosion Effects in a Train Station. *Internal Security,* **3**(1), pp. 49-62.

SUIDAN, M.T. and SCHNOBRICH, W.C., 1973. Finite Element Analysis of Reinforced Concrete. *Journal of the Structural Division,* **99**(ST10), pp. 2109-2122.

SÜMER, Y. and AKTAS, M., 2011. Bond Length Effect of Fiber Reinforced Polymers Bonded Reinforced Concrete Beams. *International Journal of the Physical Sciences,* **6**(24), pp. 5795-5803.

UNGER, J.F., ECKARDT, S. and KÖNKE, C., 2007. Modelling of Cohesive Crack Growth in Concrete Structures with the Extended Finite Element Method. *Computer Methods in Applied Mechanics and Engineering,* **196**(41), pp. 4087-4100.

WANG, N. and XU, S.-., 2011. Flexural Response of Reinforced Concrete Beams Strengthened with Post–Poured Ultra High Toughness Cementitious Composites Layer. *Journal of Central South University of Technology,* **18**(3), pp. 932-939.

WELLS, G.N. and SLUYS, L.J., 2001. A New Method for Modelling Cohesive Cracks Using Finite Elements. *International Journal for Numerical Methods in Engineering,* **50**(12), pp. 2667-2682.

WILLIAM, K.J. and WARNKE, E.P., 1975. Constitutive Model for the Triaxial Behavior of Concrete, *International Association for Bridge and Structural Engineering* 1975, ISMES, pp. 174.

YANG, Z.J. and CHEN, J.F., 2005. Finite Element Modelling of Multiple Cohesive Discrete Crack Propagation in Reinforced Concrete Beams. *Engineering Fracture Mechanics,* **72**(14), pp. 2280-2297.

YU, T., TENG, J.G., WONG, Y.L. and DONG, S.L., 2010. Finite Element Modeling of Confined Concrete-I: Drucker–Prager Type Plasticity Model. *Engineering Structures,* **32**(3), pp. 665-679.

YU, X. and HUANG, Z., 2008. An Embedded FE Model for Modelling Reinforced Concrete Slabs in Fire. *Engineering Structures,* **30**(11), pp. 3228-3238.

YU, R.C. and RUIZ, G., 2006. Explicit finite element modeling of static crack propagation in reinforced concrete. *International Journal of Fracture,* **141**(3-4), pp. 357-372.

ZANGENEH KAMALI, A., 2012. *Shear Strength of Reinforced Concrete Beams Subjected to Blast Loading: Non–linear Dynamic Analysis*, Royal Institute of Technology (KTM), Division of Structural Engineering and Bridges, Stockholm, Sweden.

ZHU, W.C. and TANG, C.A., 2002. Numerical Simulation on Shear Fracture Process of Concrete using Mesoscopic Mechanical Model. *Construction and Building Materials,* **16**(8), pp. 453-463.

ZIRABA, Y.N., BALUCH, M.H., BASUNBUL, I.A., AZAD, A.K., AL-SULAIMANI, G.J. and SHARIF, A.M., 1995. Combined Experimental–Numerical Approach to Characterization of Steel–Glue–Concrete Interface. *Materials and Structures,* **28**(9), pp. 518-525.